VARIABLE STIFFNESS STRUCTURES VIA MECHANICS MODIFICATION AND ANTAGONISTIC ACTUATION IN SOFT ROBOTIC MATERIALS

By

EMILY A. ALLEN

A thesis submitted in partial fulfillment of
the requirements for the degree of

MASTER OF SCIENCE IN MECHANICAL ENGINEERING

WASHINGTON STATE UNIVERSITY
School of Mechanical and Materials Engineering

MAY 2020

To the Faculty of Washington State University:

The members of the Committee appointed to examine the thesis of EMILY A. ALLEN find it satisfactory and recommend that it be accepted.

John Swensen, Ph.D., Chair

Arda Gozen, Ph.D.

Roland Chen, Ph.D.

ACKNOWLEDGMENT

First and foremost, it is my greatest joy to acknowledge my heavenly father who created me and walks beside me in every season of life. It is by His grace alone that I am saved and given purpose in life.

I would like to express my sincere gratitude toward my research advisor Dr. John Swensen for offering guidance in my research, inspiring my curiosity, and pushing me toward my goals.

I am also grateful to other faculty members at WSU who contributed ideas and insight for my research endeavors, specifically Dave Torick and Dr. Lloyd Smith.

My parents are beyond deserving of thanks for their selfless support, prayers, wisdom, and encouragement throughout my life. My dad's contagious enthusiasm for engineering first piqued my interest in the subject.

Finally, I have been richly blessed by my roommates who never fail to provide encouragement and distraction when needed most.

This work would not have been possible without the financial support provided by the National Science Foundation's National Robotics Initiative (Award#1734117).

VARIABLE STIFFNESS STRUCTURES VIA MECHANICS MODIFICATION AND ANTAGONISTIC ACTUATION IN SOFT ROBOTIC MATERIALS

Abstract

by Emily A. Allen, M.S.
Washington State University
May 2020

Chair: John Swensen

The soft robotics approach seeks to provide the efficiency and autonomy of robots while using soft materials that are safe for interaction with humans and delicate objects. The inherent weakness of flexible materials renders ordinary usage of soft materials inadequate for robots that need to exert large forces.

In this paper, two classes of mechanisms for variable stiffness structures are explored: intrinsic variable stiffness and dual antagonistic actuation. This work proposes designs and modeling strategies for variable stiffness structures that incorporate smart materials (to enable modification of intrinsic mechanical properties), geometric patterning of low melting point materials (to enable directional stiffness control), and pneumatic/shape memory alloy antagonistic actuation (to enable independent control of stiffness and bending). Whereas other researchers have focused on controlling the magnitude of stiffness in soft materials, this paper also explores soft robotic structures with directional stiffness control.

The mechanical properties of the materials are tested via tension, compression, and 3-point bend tests. Kinematic modeling of the patterned structure relies on the product of exponentials method for serial link robots, then incorporates tendon forces and selectable axes for the kinetic relationships. A finite element model is constructed in MATLAB to predict the configuration of the pneumatic/shape memory alloy actuator based on measured material properties. Each of the proposed designs are fabricated and tested to demonstrate their variable stiffness capabilities and compare with modeling results.

TABLE OF CONTENTS

CHAPTER

APPENDIX

LIST OF TABLES

LIST OF FIGURES

Dedication

This thesis is dedicated to my parents whose support and enthusiasm fueled my passion for learning.

Chapter One

INTRODUCTION

Attribution:

This chapter is original work written by Emily Allen.

1.1 Soft Robotics

With the persistent demand for increased task efficiency and automation in today's advancing technological society, robots are becoming increasingly prevalent, particularly in the manufacturing realm. Robots excel at performing repetitive tasks at impressive speeds with high precision and consistency. However, these industrial robots are usually limited to operation in isolated environments as their heavy, rigid components pose safety hazards for humans within the work space of the rapid-moving machines.

Recently, there has been a push for robots that can operate in less restricted environments, even alongside humans as collaborative robots (cobots). This requires robots to respond well to uncertainty as they perform in less predictable environments with safety as a high priority. These objectives have motivated a surge of research over the last two decades, shifting the entire paradigm around robot materials and structures. Traditional robots consist of heavy, rigid parts driven by high power motors which are unsuitable for cobot applications. Thus, a new field emerged with the name soft robotics to distinguish from traditional hard robots, classified based on the underlying materials. Iida and Laschi [1] describe soft robotics as a field with multiple facets including the investigation of unconventional materials and autonomous system morphologies, the defining of relationships between morphologies and funcionalities, and the undertaking of challenges such as self-stability,-organization, and -assembly. Soft robots usually encompass flexible rubbers or other polymers for cushioning/gripping, sometimes accompanied by superelastic materials or other embedded smart materials. These soft materials can conform to ill-defined surfaces, distribute impact forces, and absorb shock, thus improving collision safety as reviewed by Kim et al. [2]. Laschi and colleagues note that the deformable nature of the soft materials combined with creative actuation strategies enable soft robots with squeezing, stretching, climbing, and morphing capabilities that would be infeasible for their rigid counterparts [3]. With the implementation of highly-functional soft materials, robot applications have now extended to a new realm including wearable assistive devices, prosthetics, soft tools for minimally-invasive surgeries, soft wall-climbing robots, and soft grippers for delicate objects [4].

1.1.1 Biological Inspiration

Many researchers look to nature as inspiration for soft robot design. Biological examples abound in adept creatures whose soft tissue and musculature are their primary means of structure and actuation.

Numerous hydrostatic mechanisms exist in nature, where the configuration of a biological structure is controlled by fluid pressure gradients and the underlying geometry of the constraints. Examples of biological members that utilize such mechanisms include the elephant trunk, the human tongue, squid tentacles, and carnivorous plants such as the Venus flytrap. These unique actuation mechanisms allow the flexible structures to morph into various configurations with substantial strength without need of skeletal support [5–8]. Mimicking this remarkable capability is a sought-after objective for many soft robotics research efforts.

Mimicry of other biological feats such as worm locomotion and intestinal peristalsis have also been attempted with soft robots [9–11]. Kim et al. notes that caterpillars can stiffen their body to cross a chasm by increasing their internal pressure [2].

Although mimicking complicated biological organisms is a challenging task, basic concepts from these adept structures can be incorporated in simplistic soft robotic elements. The regulation of a pressure gradient between layers, and the muscle fiber arrangement and fluid incompressibility seen in the muscular hydrostats show great promise for application in the soft robotics research field where flexible, high strength movements are the main objective.

1.1.2 Actuation

Unlike traditional robots which typically have an actuator for every discrete joint, soft robot actuators are usually distributed throughout the structure, forming holistic actuator structures; this "prevents the use of many traditional hard actuators such as electric motors in soft robots [12]." As reviewed by Kim et al., most alternative actuation strategies fall into three general categories: dielectric elastomeric actuators (DEA's), shape memory alloy actuators (SMA's), and pressurized fluid actuators [2].

Dielectric elastomers exhibit shape change when a potential difference is applied across electrodes on opposing surfaces. These actuators are biocompatible, soft, and flexible by nature, and they have a fast response time compared to other actuators [13, 14]. The dielectric effect also enables self-sensing through feedback signals, although they require high voltage, careful fabrication, and are susceptible to dielectric breakdown when charge leaks across the dielectric, especially at flaws in the material [15, 16].

Shape memory alloy wires are a popular choice for soft actuators due to their high strength-to-weight ratio. Thin wires can be easily embedded into robotic structures to produce desirable motions upon heating/contraction of the wire. Although the material itself is limited to low strain ($\sim 5\%$), forming the wire into small springs enables much larger strains albeit with some compromise in strength [2, 17].

Fluidic actuation has also been employed to create high power soft actuators that are deformed by pressurized air or other fluid [2, 18]. This method can produce large forces and displacements [19–21], although networks of supply tubing add complexity to large-scale systems.

1.1.3 Challenges with Soft Robots

Unfortunately, the most advantageous feature of soft robots—their soft, flexible nature—is also their greatest drawback. The compliant materials that make soft robots able to squeeze through tight spaces, morph around unknown obstacles, and deform upon impact also hinder them from exerting substantial forces. The strength challenge is not the only obstacle that impedes functional soft robots. Lee et al. points out that soft robots' deformable nature challenges the use of rigid sensors such as encoders and strain gauges [13]. Due to the infinite degrees of freedom introduced by continuum actuators, conventional control strategies are often unsuitable for soft robots [1, 13]. New methods are required for modeling soft robots as their continuous deformation cannot be decribed with traditional rigid body analysis [1, 2]. Modeling of soft structures must account for nonlinear material properties and viscoelastic effects [22]. Thermally activated systems often suffer slow response time due to sluggish heat dissipation exacerbated by insulative soft materials. Furthermore, many actuation methods are deemed impractical due to high voltage requirements, strain limitations, and lack of scalability [23].

1.2 Variable Stiffness Structures

Many robots are successfully designed for specific tasks. These robots can function well with conventional rigid or soft components, depending on the task they're design for. However, more broadly-capable, lifelike robots need to be able to perform diverse tasks. For example, such robots might require the softness to rearrange delicate objects yet also need the strength to lift heavy objects. This mechanical versatility cannot be achieved with any single standard material. A material strong enough to exert large forces would damage the delicate objects, and likewise a material soft enough to handle delicate objects would collapse under a heavy load. Majidi termed this concept 'compliance matching': "the principle that contacting materials should share similar mechanical rigidity in order to evenly distribute internal load and minimize interfacial stress concentrations [24]." Majidi also notes that hard plastics and metals have elastic moduli on the order of 10^9 Pa while skin/muscle tissue usually have moduli in the range of $10^2 - 10^6$ Pa. This results in a severe ‘compliance mismatch’ when rigid robots attempt to interact with humans, animals, and other soft objects, resulting in stress concentrations, damage to delicate objects or organs, and interference with natural motions [24].

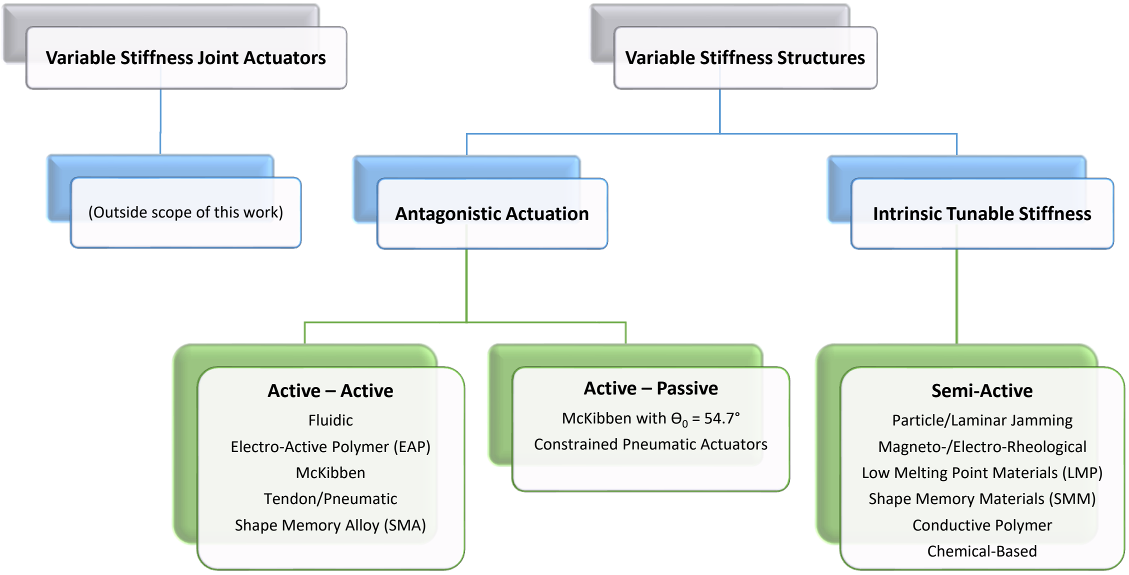

Figure 1.1 Classification of variable stiffness structures and actuators using categories modified from review by Manti et al. [25].

In order to achieve compliance matching for a variety of tasks, soft robots need a deformability/compliance that is both variable and controllable [25]. Manti and colleagues conducted a thorough review of variable stiffness structures which can be categorized into two broad categories: antagonistic actuation and intrinsic tunable stiffness [25]. An important distinction is drawn between variable stiffness structures—whose total framework stiffness may be controlled—and variable stiffness joint actuators—which modulate the stiffness of joints between semi-rigid links [26–28]. The latter falls outside the focus of this work.

1.2.1 Antagonistic Actuation

Antagonistic actuation involves either active elements in opposing directions (active-active) or active elements paired with passive structures that prevent deformation (active-passive) [25].

The active-active arrangement consists of an opposing arrangement of soft actuators in a single structure to enable independent control of motion and stiffness. This arrangement can be created with virtually any soft actuator technology or combination thereof. Activating any single actuator or asymmetric grouping causes motion, but simultaneous activation of antagonistic actuators results in increased stiffness with no deformation. These motion-inducing and stiffening effects can be combined by activating opposing actuators in uneven groupings. Multiple fluidic actuators such as McKibben actuators, which contract in length when pressurized, can be antogonistically arranged to achieve increased stiffness when simultaneously activated. To this end, fluidic actuators can also be paired with other actuation mechanisms. For example, some have combined a central pneumatic actuator with tendons along the sides to restrain the device when high stiffness is desired [29–31]. SMA bundles which shorten when heated can be arranged to constrain a structure both longitudinally and in the transverse direction, similar to the muscles in octopus limbs [32–34]. Dielectic eleastomer actuators (DEA's) are the most common application of electroactive polymers (EAP's) in the soft robotics field. The electrostatic pressure generated between electrodes from the Coulombic forces squeezes the elastomer, resulting in elongation. Creative stacking and folding arrangements of these actuators can facilitate variable stiffness via electrical activation [35, 36].

The active-passive arrangement involves a soft actuator with constraints imposed by a passive structure. For example, McKibben actuators whose sleeve is woven at an angle of exactly 54.7° are unable to expand or contract due to the fiber restraint. As a result, pressurization of these actuators results in stiffening rather than motion [37]. These passive stiffening actuators can be combined in parallel with McKibben actuators to produce both motion and stiffness control [38]. Active-passive variable stiffness structures are not the focus of this work and will not be further discussed here.

1.2.2 Intrinsic Tunable Stiffness

Structures with intrinsic tunable stiffness exhibit variable stiffness via mechanics modification of the material itself. This may be achieved in a variety of ways, each involving some sort of external stimulus—whether heat, pressure, chemical, or electric/magnetic field—to instigate a change in material properties.

Jamming-based structures contain either fine particles or thin, flexible sheets in a sealed chamber. Under neutral pressure, the particles or laminae slide freely and allow flexible, soft behavior. By drawing a vacuum on the chamber, the particles or laminae are jammed together, and the increased friction causes resistance to deformation, resulting in a high stiffness state [39–42].

Magnetorheological and electrorheological materials are fluids whose rehological properties are altared by the presence of a magnetic or electric field. These fluids can be encapsulated in chambers within a soft material to enable stiffness variability as demonstrated in [43]. More commonly, this concept is exploited by directly embedding ferromagnetic or ferroelectric particles in an elastomer during curing [44].

Conductive polymers can conduct electricity via carbon black powder infused in the polymer [45]. Joule heating of the entire material then softens the polymer.

Chemically-stimulated materials are primarily based on hydro absorption. Certain polymers exposed to water demonstrate slow but significant softening upon hydration [25, 46].

The stiffness of low melting point (LMP) materials is dramatically changed when the material softens or melts under a heat stimulus. LMP polymers, metals, and wax have proven to be well-suited for variable stiffness soft robotic materials [47–50]. Most of these options require encapsulation in an elastomer to contain the LMP materials in their liquid state [51].

Shape memory materials (SMM's)—both polymers and metal alloys—can also be used as variable stiffness structures [52]. Although SMM's are more commonly known for their actuation usages, the phase change responsible for the shape memory effect also causes a substantial change in Young's modulus. Nitinol, for example, an alloy of Nickel and Titanium, transforms from martensite to austenite when heated above its transition temperature. In the low temperature martensite phase, the metal is soft and flexible; but when heated and transformed to austenite, the material becomes much stiffer and resistant to plastic deformation [53].

1.3 Objective and Contents Overview

The present work is multifaceted, focusing on both the active-active antagonistic actuation and the semi-active intrinsic tunable stiffness categories defined above. A review of closely-related seminal works is included in each chapter to highlight the relevance and uniqueness of each concept.

Chapters 2 and 3 focus on the investigation and design of materials whose magnitude and direction of stiffness may be controlled. While other tunable stiffness materials have included SMA's and LMP materials to achieve a thermally activated stiffness change, smart composite materials are proposed in chapter 2 which combine multiple smart materials in a single composite to enable finer stiffness control. The proposed materials are tested in flexure to compare the composites' stiffness behavior with that of the individual constituent materials.

In chapter 3, the concept of embedded LMP materials for intrinsic stiffness variability is extended to incorporate geometric patterning. While the smart material composites from chapter 2 emphasize the ability to control the magnitude of stiffness, the LMP lattice structures proposed in chapter 3 introduce directional stiffness control. The forward kinematics relationships and kinetic modeling of the structure are developed and demonstrated with the physical test piece.

Chapter 4 presents a new embodiment of the active-active antagonistic actuation arrangement. Here the SMA and pneumatic soft actuation technologies are combined to enable variable stiffness as well as directional bending control. A finite element model is developed to describe the bend curvature as a function of internal pressure and SMA activation. The actuators are fabricated, tested, and compared with the proposed finite element model.

Chapter 5 summarizes the major findings from chapters 2-4, discusses the main challenges, and presents recommendations for related future work.

Chapter Two

SMART MATERIAL COMPOSITES

Attribution:

This chapter is a modification of two original papers previously published.

Contributions from:

John P. Swensen[1], Lee D. Taylor[1]

[1]School of Mechanical and Materials Engineering, Washington State University, Pullman, WA

This text is published with the following citations:

E. A. Allen, L. D. Taylor, and J. P. Swensen, “Smart material composites for discrete stiffness materials,” *Smart Materials and Structures*, vol. 28, no. 7, p. 074007, Jun. 2019.

E. A. Allen, L. D. Taylor, and J. P. Swensen, “Smart material composites for discrete stiffness materials,” in Proc. *ASME 2018 Conference on Smart Materials, Adaptive Structures and Intelligent Systems (SMASIS2018)*, San Antonio, TX, 2018, p. V002T06A015.

2.1 Abstract

This paper presents an initial step towards a new class of soft robotics materials, where the combination of multiple smart materials can exhibit discrete levels of stiffness. This work is inspired by a variety of biological systems where actuation is accomplished by modulating the local stiffness in conjunction with muscle contractions. Whereas most biological systems

use hydrostatic mechanisms to achieve stiffness variability, and many robotic systems have mimicked this mechanism, this work aims to use smart materials to achieve this stiffness variability. Here the compositing of the low melting point Field's metal, shape memory alloy Nitinol, and a low melting point thermoplastic Polycaprolactone (PCL), composited in simple beam structure encased in silicone rubber is presented. A simple two-joint soft robotic finger is constructed to demonstrate the dexterous capabilities of smart composite materials. The comparison in bending stiffnesses at different temperatures, which reside between the activation temperatures of the composited smart materials demonstrates the ability to achieve discrete levels of stiffnesses within the soft robotic tissue.

2.2 Introduction

Soft robotics and compliant robotic mechanisms have gained increasing popularity in the past decade within the academic community. This soft robotics approach is in stark contrast to the traditional paradigm of large, heavy, rapidly-moving robotics in isolated environments. The soft-robotic approach has shown promise because their compliant nature lends itself well to safety concerns in co-robotics environments and exhibits adaptability and robustness to uncertainty, such as in robotic grasping. However, this same intrinsic compliance in soft robotics is also its greatest drawback — in many scenarios it is unable to exert necessary forces and control manipulator shape under external loading.

However, biological systems abound where the primary method of actuation is the ability to adjust the stiffness of tissues in conjunction with localized muscle contractions. These types of actuation methods are widely prevalent in the muscular hydrostats, catch muscles, and catch connective tissues in cephalopods and echinoderms [54, 55]. This combination of co-located muscle and adaptive tissue provide these animals with the ability to squeeze through holes much smaller than their average body diameter and capture or crush their prey. The primary focus of this paper is the development of new techniques in the compositing of

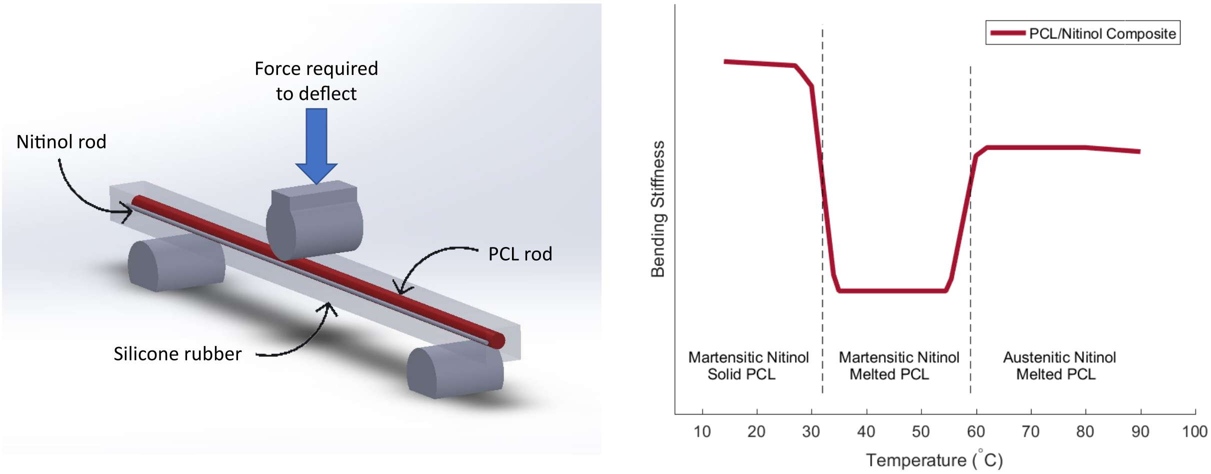

Figure 2.1 Bend test setup (left) and three discrete stiffness regions expected for composite of Nitinol and PCL rods encased in a silicone rubber matrix (right).

existing soft-robotic technologies and carefully designed geometry of smart material additives to create robotic components with the ability to switch between acting as soft robots or traditional rigid robots, approaching the extreme capabilities of their biological counterparts, by presenting multiple discrete levels of stiffness.

Traditionally, robotic systems have followed the paradigm of being comprised primarily of rigid structures with relatively few degrees of freedom and well-characterized motion driven by actuators directly connected to the rigid links. In recent years, there has been an explosion of research in the area of soft robotics, as they provide the promise of allowing robots and humans to work and collaborate in the same workspace. Additionally, soft robotics has proven to be an ideal testbed for taking inspiration from biological systems, as described above, and including them in soft robotic designs that exhibit either bio-mimicry or bio-inspiration [3, 56–58]. However, soft robotics have inherently limited ability to exert forces and interact with their surroundings in a meaningful way because of their compliant nature. Hence there is a great need for materials and mechanisms that have the ability to dynamically change between acting as a soft or a rigid robotic component.

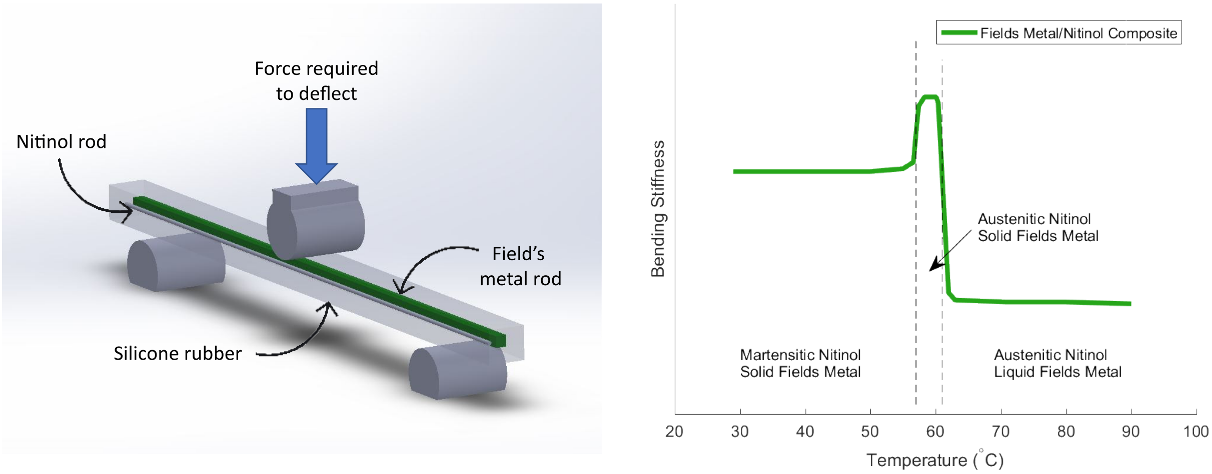

Figure 2.2 Bend test setup (left) and three discrete stiffness regions expected for composite of Nitinol and Field's metal rods encased in a silicone rubber matrix (right).

2.2.1 Variable stiffness actuators

Many variable stiffness actuators require complex design and machining to achieve a change of stiffness in even a single degree of freedom [28, 59–61]. These often involve a high degree of complexity in terms of motors, mechanisms, and/or cable routings. Other approaches require high bandwidth feedback control to render a variable stiffness through a control system [27, 62]. These approaches are usually not scalable and are more targeted at applications with a distinct drive train, rather than as material actuators and structures. However, when amenable these approaches provide the highest fidelity of rendered variable stiffness.

2.2.2 Variable stiffness structures

Tensile integrity, or tensegrity, structures were initially used in architecture and artwork, with the term coined by Buckminster Fuller. It is characterized by systems of struts and cables where all of the cables have been prestressed and struts are either in compression or tension, thus maintaining the structural integrity of the whole. When applied to robotic systems, these tensegrity structures are designed such that the robot can selectively release tension in one or more cables, resulting in a predictable motion during collapse. Sequential loading and unloading of the cable generates reproducible gaits [63, 64]. Other researchers are focusing on the valid tensegrity configurations that result in predictable deformations and their associated control [65, 66].

2.2.3 Soft Robotic Actuators

The majority of soft robotics, both actuators and systems, are primarily concerned with the problem of compliance matching to the task of the robotic system [24]. This aim is often accomplished through purely elastomeric materials—some with embedded sensing technologies—or with geometrically-complex chambers and pneumatic controls to deform an elastomer when the chambers are pressurized [12, 67–69]. Many biomimetic robots have utilized pneumatic artificial muscles optimized for specific tasks and applications [37, 38, 70, 71]. These actuators closely match the architecture of human muscles but are generally connected to rigid links which lack the compliance necessary for some applications [72]. Antagonistic arrangements of pneumatic actuators has enabled some stiffness variability in robotic gripping devices [73]. Previously, other geometric approaches to compliance were dominated by tendon driven robots with compliant backbones [33, 74–76]. More recently, origami approaches to generating compliant mechanisms have also been employed [77].

Other recent efforts which are similar to the proposed work involve the combination of heaters and low-melting point metals, but these methods are restricted to a very thin geometry and global heating [78–80]. Other research using low melting point metals were focused on creating fabrics and threads with changeable stiffness [45, 81]. Shape-memory-alloys and shape-memory-polymers have also been combined to create variable-stiffness fabrics and fingers with self-actuation capabilities [82, 83]. The work presented in this paper is a first step towards the long term goal of stiffness control in magnitude, directionality, and spatial resolution. The focus is no longer just on the method of stiffening, as reviewed by Manti and Elango et al. [22, 25], but on how the compositing of multiple materials can result in multiple discrete stiffness levels within the same composite, as illustrated in Figures 2.1 and 2.2.

2.3 Methods

Rods of Nitinol, PCL, and Field's metal (FM) are embedded in silicone rubber to form composite beams with variable stiffness due to the smart behavior of the constituent materials. 3-point bend tests are conducted on the composite beams and the individual materials at temperatures spanning all three levels of discrete stiffness. Samples are held at constant temperature throughout each test which spans both the elastic and plastic range of deformation.

2.3.1 Smart Materials

As shown in Table 2.1, each smart material used in this experiment exhibits a distinct change in stiffness at a specific critical temperature. This notable change in behavior can be explained by a change in microstructure or melting of the material. The critical temperatures and flexural modulus values listed in Table 2.1 were extracted from data from the 3-point bend tests conducted on each material at constant temperature in this experiment. These values are evidenced by the data in Figures 2.7, 2.8, and 2.9.

Table 2.1 Stiffness variability of individual smart materials.

Smart material	Critical temperature	Stiffness variability
Nitinol	50-60 °C martensite to austenite	18 GPa to 65 GPa
PCL	30-50 °C melting temperature range	200 MPa to 0 MPa
Field's metal	62 °C melting temperature	5 GPa to 0 GPa

Nitinol

Nitinol is a nickel-titanium alloy that exhibits the shape-memory effect. Above the austenite finish temperature, the nitinol becomes austenitic, increasing stiffness and making it resistant to deformation. Below the martensite finish temperature, this shape memory alloy transforms to a twinned martensite structure. Applying load to the material in its twinned martensite phase causes elastic deformation followed by de-twinning of the martensite. This de-twinning process results in pseudo-plastic deformation up to 7% strain. When the material is reheated above its critical temperature, it returns to its initial shape as it transforms to austenite. This unique behavior is desirable for variable stiffness composites as it offers high stiffness at high temperatures where most materials become softer or melt. Chemically pickled shape memory Nitinol wire from Confluent Medical (P/N WSM007500000SE) was used for this experiment. This particular wire was observed to transform from martensite to austenite between 50 and 60 °C.

PCL

Polycaprolactone (PCL) is a polyester that melts between 30-50 °C with a glass transition temperature of about 60 °C. Unlike the instantaneous liquification of some materials, PCL softens gradually over a broad temperature range. It softens substantially before reaching its melting temperature, and even after melting completely PCL remains extremely viscous. This transformation from a relatively rigid room temperature solid to a viscous melt at a slightly elevated temperature offers desirable behavior for varying stiffness at relatively low temperatures.

Field's metal

Field's metal is a low melting-temperature eutectic alloy that melts uniformly at 62 °C. It is comprised of 51% indium, 32.5% bismuth, and 16.5% tin by weight. Field's metal is relatively soft compared to other metals with an elastic modulus much lower than that of aluminum and other metals. It's low melting temperature lends itself to stiffness variability within a reasonable temperature range. Bismuth Indium Tin ingot Field's metal (stock number 46895) from Rotometals was used for this experiment.

2.3.2 Test sample preparation

To prepare the PCL rods for samples (b) and (e) from Figure 2.3, six strands of 2.85mm diameter low temperature PCL filament were cut to length, twisted around each other, and heated to a temperature just over 60 °C using a hand held heat gun. The heated strands were then rolled together by hand until the individual strands fused together, producing a uniform rod with a nominal diameter of 7.2mm.

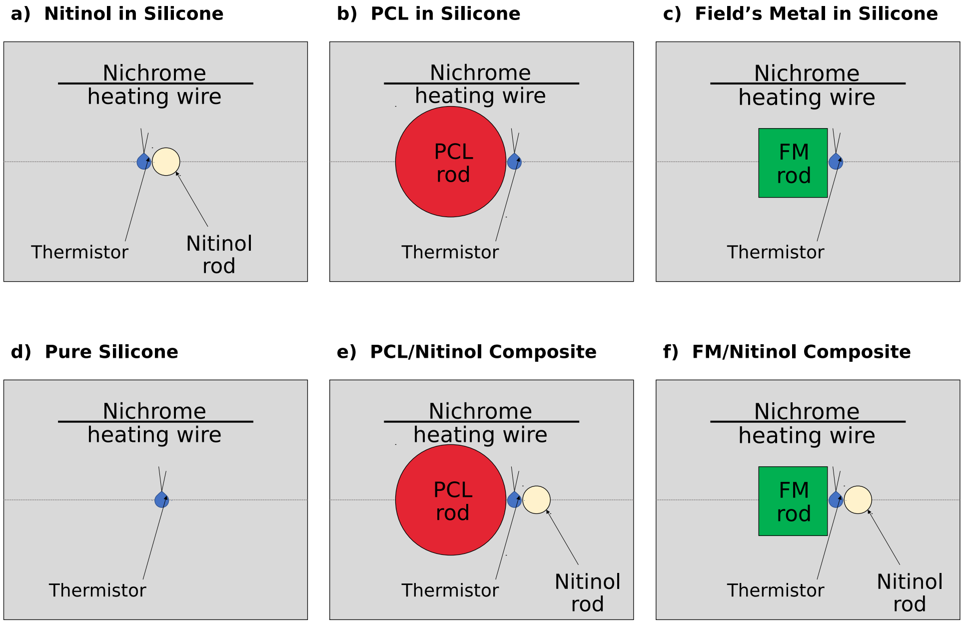

Figure 2.3 Cross-sectional diagram of composite samples fabricated for bend tests. Three of each sample were fabricated to verify repeatability between samples in the testing.

For the PCL/Nitinol composite, a PCL rod and an identical length of 1.91mm diameter Nitinol were positioned side-by-side in the center of an 18mm wide x 16.75mm high mold.

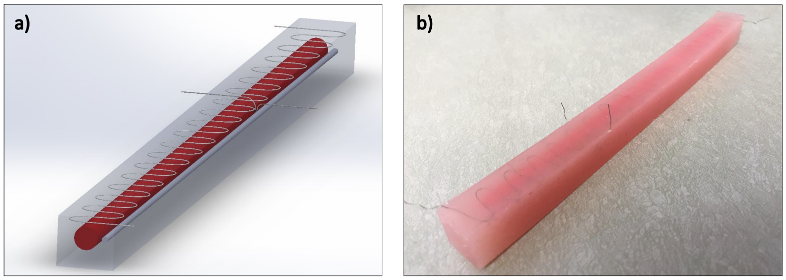

Figure 2.4 Trimetric view of composite sample showing serpentine pattern of nichrome heating element (a), and photo of physical composite sample (b).

An NTC 10K thermistor was situated snugly between the two rods. A Nichrome heating element formed into a serpentine pattern, was embedded above the rods to provide uniform Joule heating of the composite beam. The $^{\text{TM}}$ Dragon Skin 20 liquid silicone was cast in layers to ensure proper spacing of the rods, heating element, and thermistor within the mold.

The Field's metal rods for use in samples (c) and (f) from Figure 2.3 were formed by melting the metal ingot and pouring the liquid metal into a 4.1mm x 4.1mm mold 3D printed with NinjaFlex brand filament. The process of compositing the FM/Nitinol sample was otherwise identical to the PCL/Nitinol composite sample previously described.

Nitinol, Field's metal, and PCL samples, intended for individual material testing, were encased in the silicone alone with the heating element and thermistor as shown in Figure 2.3(a) to (c). These samples were created using the same methods described above for the PCL/Nitinol composite, but were enclosed in silicone without the Nitinol.

A pure silicone beam for determining the properties of the matrix material itself was also cast with no internal rods, as shown in Figure 3(d).

2.3.3 Test processes

3-point bend tests were conducted on individual materials (embedded in silicone) and composite beams using a Mark-10 Force Test Stand. As specified in the ISO standard for bend testing metallic materials, the equipment is fitted with polycarbonate supports with sufficient rigidity relative to the softer materials being tested [84]. The ASTM standard for bend testing plastic materials recommends a support span of 16 times the height of the testing specimen; the outer supports are spaced in conformance to the standard [85]. The polycarbonate loading nose attached to the load cell has a 10mm curvature radius to prevent the Nitinol from deforming at sharp, unrecoverable angles.

Load-deflection curves were obtained at 7 different temperatures for each beam: 29, 40, 50, 60, 70, 80, and 90 °C. The testing temperatures were chosen to capture the behavior of the materials in each stiffness region. Prior to testing, each sample was heated to the desired temperature by passing current through the heating element and monitoring the temperature with the embedded thermistor. The sample temperature was held constant through each test by toggling the heating element power supply on/off. Load and deflection data were collected simultaneously while the indenter was lowered at 5mm/s on the center of the specimen. Samples were tested up to 40 mm center deflection to investigate stiffness behavior under both plastic and elastic deformation at each of the test temperatures. As recommended by ASTM, toe compensation was made on the collected data to correct for the taking up of slack at the beginning of each test [85]. Tests were repeated with 3 identical samples under each set of conditions to verify repeatability. Samples that underwent permanent deformation were reset between tests by heating the materials up to 85 °C and allowing them to cool to melt and re-solidify any low melting temp materials or reset the shape of the shape memory Nitinol.

2.3.4 Smart composite finger

A PCL/Nitinol composite finger was also constructed to demonstrate the unique capabilities of robots constructed with composite smart materials. The finger was fabricated similarly to the PCL/Nitinol composite beam shown in Figure 2.3, but notches in the top of the silicone were added to allow bending at two joint regions. A separate Nichrome heating element was embedded in each of the two joint segments, spanning the length of each joint. As seen in Figure 2.5, a tendon was routed through sheathes in the silicone to minimize friction and prevent tearing of the silicone.

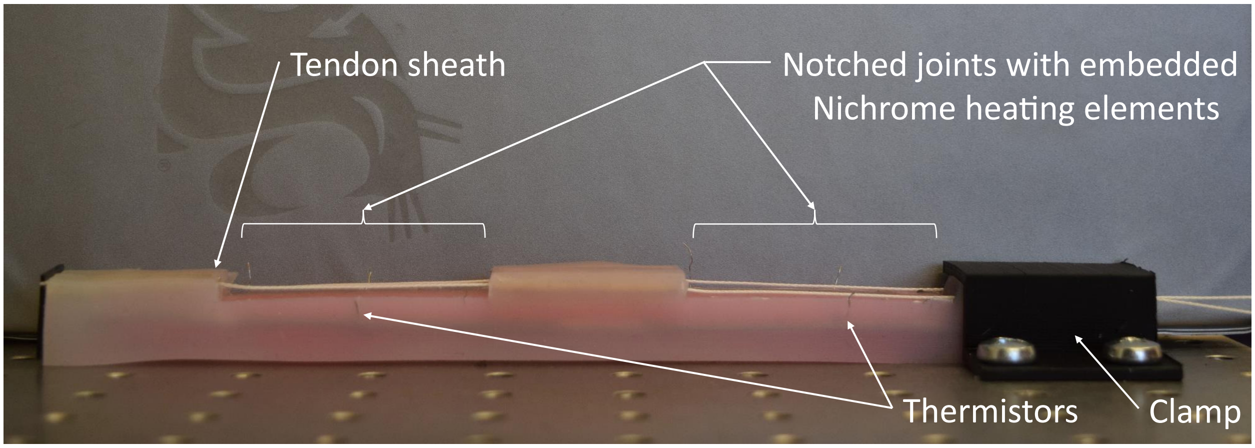

Figure 2.5 Relaxed configuration of PCL/Nitinol composite finger when tendon is slack.

By heating the joints individually to different temperatures, 9 different configurations should be achievable for any particular tendon force since each joint can exhibit 3 different stiffnesses. The tendon force is applied by manually sliding a load cell attached to the tendon along a track that keeps force application co-linear with the proximal tendon sheathes. Whereas most robotic fingers would require separate tendons for each joint to control the relative joint angles, the smart composite finger should produce various joint angle combinations with a single tendon by using temperature to control the relative joint stiffnesses.

2.4 Results

Bend testing of the individual materials and composite beams revealed the stiffness variation and critical temperatures of each sample. The flexural elastic modulus is calculated from the equation

$$E = \frac{mL^3}{4wh^3} \tag{2.1}$$

for rectangular beams, or

$$E = \frac{4mL^3}{3\pi d^4} \tag{2.2}$$

for beams with round cross sections [85]. In both Equations 2.1 and 2.2, m represents the slope of the initial linear region of the measured force-deflection curve; L is the support span and w, h, and d are the geometric dimensions of the specimens.

The load-deflection curves obtained from the constant temperature tests are plotted for each individual and composite material. These plots, shown in Figure 2.6, are used to characterize the materials' behavior under both elastic and inelastic loading. The Nitinol, PCL, and Field's metal were all encased in silicone for testing to maintain their shape when tested above the melting points. However, the characterization of the smart materials themselves is desired, so the measured loads from the pure silicone sample were subtracted from the loads measured for the Nitinol, PCL, and Field's metal embedded in silicone to isolate the loads incurred by the smart materials themselves. This subtraction method relies on the assumption that the volume of silicone occupied by the smart material rods is negligible. In other words, the bending stiffness of the pure silicone beam is not significantly different than the bending stiffness of the silicone encasing the smart materials because the hollow channels occupied by the smart materials in the silicone are relatively narrow and are positioned along the nuetral axis. To verify this assumption, the bending inertia of the solid silicone beam and a silicone beam with hollow channels matching the dimensions of the encased smart material rods were calculated and compared. These inertia values differed by less than 2%, so this assumption should not significantly affect the results. The load-deflection curves shown in Figures 2.6(a) to 2.6(c) show the loads incurred by the smart materials themselves, with the effects of the silicone matrix subtracted from the plotted results.

These results are converted to elastic modulus values using equations 2.1 and 2.2, where m is extracted from the load-deflection curves by evaluating slope of the initial, linear range of deformation. Figures 2.7, 2.8, 2.9, and 2.10 show the temperature dependence of the elastic modulus values of the individual materials based on the geometric dimensions of the individual materials. The temperature-dependent moduli of the composite beams are shown in Figures 2.11 and 2.12; the moduli shown in Figure 2.11 and 2.12 are calculated based on the outer dimensions of the rectangular composite beams.

Vertical error bars in each of the plots represent repeatability error calculated as the standard deviation of the mean values from 3 identical tests conducted on separate samples. The thermistors used to measure temperature have a nominal random uncertainty of ±0.3 °C; however, additional uncertainty exists in these measurements due to the thermal gradient across the samples. The maximum thermal gradient across the width of the smart material rods was measured to be 2°C when the samples were held at 90°C. A much higher temperature gradient exists across the width of the entire silicone beam, but this gradient is insignificant since the stiffness of the silicone does not change substantially with temperature. Thus, the uncertainties in the temperature measurements reflect both the accuracy of the thermistor readings and the temperature gradient across the smart material rods, resulting in a total uncertainty of ± 2.02°C in all temperature measurements. Deflection measurements have minimal uncertainty in the load-deflection data collected at constant temperature because zeroing the load cell and performing toe compensation removes any bias error from the data.

2.4.1 Nitinol

As seen in Figure 2.6(a), the force required to deflect the Nitinol varies significantly with temperature. The pseudo-elastic behavior is seen in the long linear portions of the curves from the 80 and 90 °C tests. The similarity between the 29, 40, and 50 °C curves suggests that the Nitinol has hardly begun to transition to austenite at 50 °C; this indicates that complete transformation occurs at a higher temperature. The flexural elastic modulus of the Nitinol shown in Figure 2.7 exhibits two distinct levels of stiffness with a visible jump between the two levels at the transition from martensite to austenite between 50 and 60 °C.

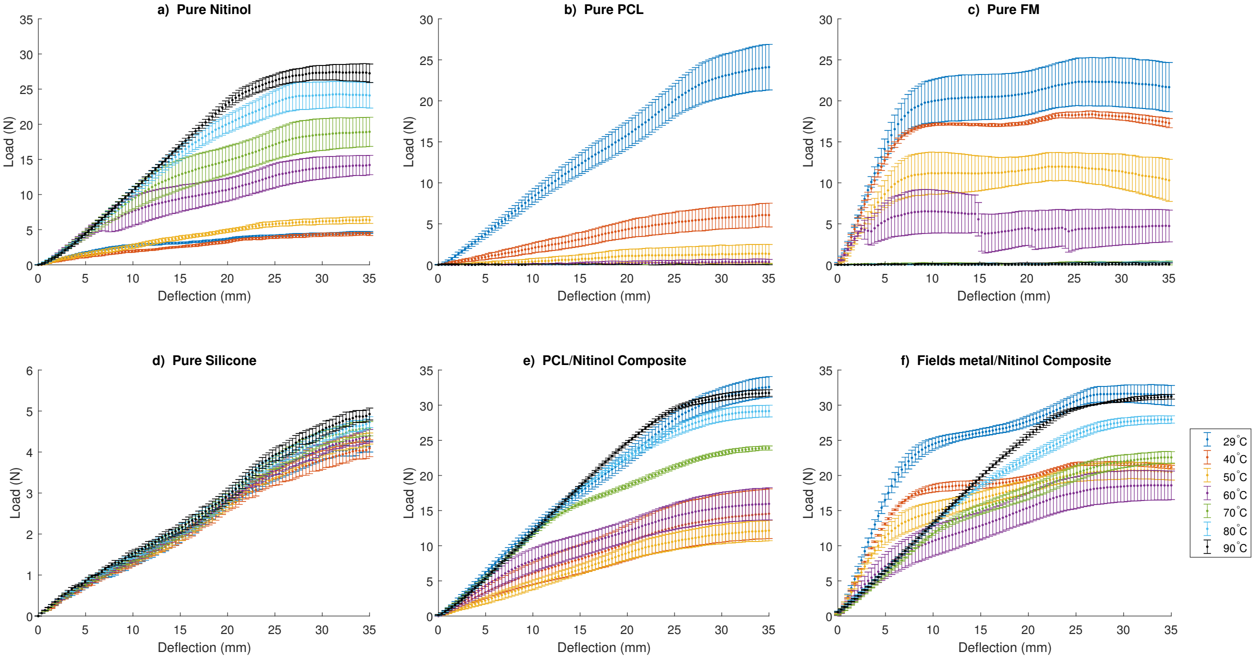

Figure 2.6 Load-deflection curves for each individual and composite sample. Vertical error bars represent repeatability error between 3 tests conducted at each temperature.

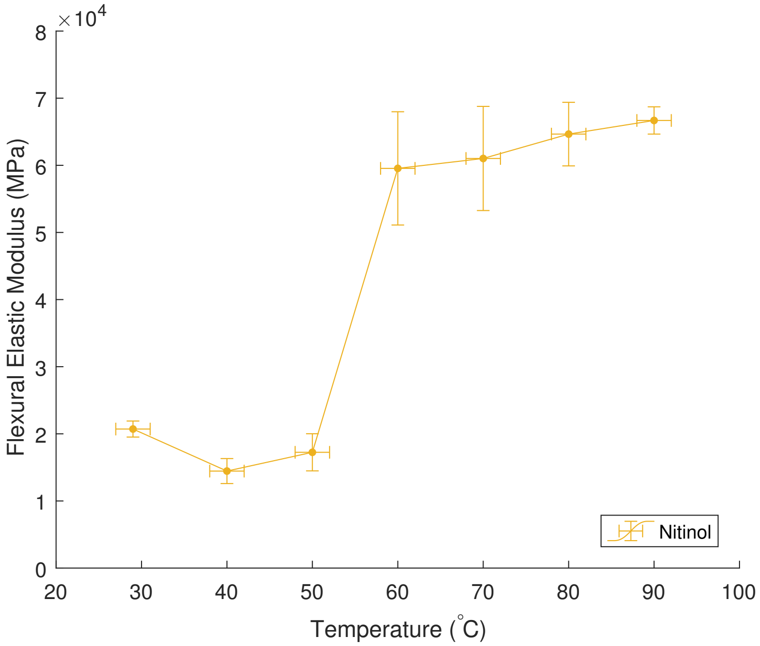

Figure 2.7 Flexural elastic modulus of pure Nitinol measured at a constant elastic deflection over a range of temperatures. The modulus values were obtained using the slopes of the load-deflection curves in Figure 2.6(a).

2.4.2 PCL

The PCL bend tests were conducted on a PCL rod encased in silicone. The load measurements from the pure silicone tests in Figure 2.6(d) are subtracted from the PCL/silicone load-deflection data to isolate the load incurred by the PCL itself, shown in Figure 2.6(b). The silicone load values can be subtracted directly without scaling since the pure silicone beam and the silicone encasing the PCL rod have equal dimensions. Repeatability error from the two sets of collected data are combined in quadrature to account for error propagated in this subtraction.

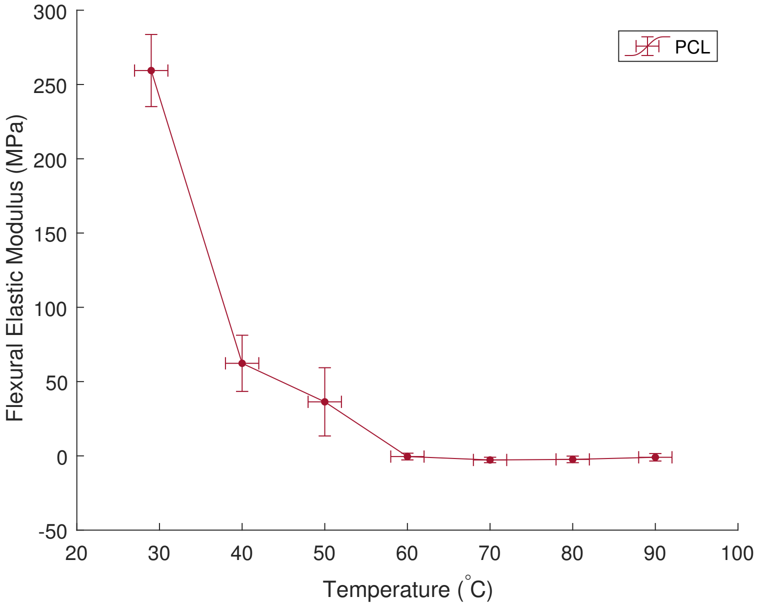

Figure 2.8 Measured flexural elastic modulus of pure PCL rod as a function of temperature. The modulus values were obtained using the slopes of the load-deflection curves in Figure 2.6(b).

The PCL rod shows a drastic change in strength and stiffness between the 29 and 40 °C tests seen in Figure 2.6(b). The elastic moduli shown in Figure 2.8 show that the rod becomes essentially limp at temperatures beyond 50 °C, suggesting that the PCL melts gradually between about 30 and 50 °C. When heated beyond its melting temperature, the PCL turns into a viscous melt, thus the modulus platteaus at temperatures between 60 and 90 °C.

2.4.3 Field's metal

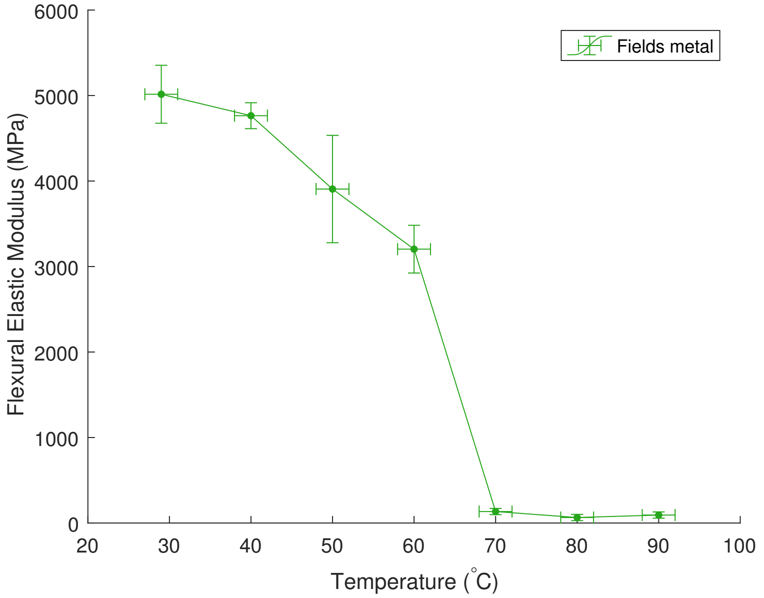

Figure 2.9 Measured flexural elastic modulus of pure Field's metal rod as a function of temperature. The modulus values were obtained using the slopes of the load-deflection curves in Figure 2.6(c).

The Field's metal bend tests were conducted on a Field's metal rod encased in silicone since testing cannot be conducted on a material in its liquid state if it is not encased in a matrix material. Just as in the case of the PCL, the load measurements from the pure silicone load-deflection data, shown in Figure 2.6(d) are subtracted from the Field's metal/silicone load data to isolate the load incurred by the Field's metal itself, shown in Figure 2.6(c). Repeatability error from the two sets of collected data are again combined in quadrature.

A sharp melting point is expected from the Field's metal due to its eutectic nature. As seen in Figure 2.9, the Field's metal shows some gradual decrease in overall strength when heated from 29 to 60 °C, and a significant drop in stiffness when heated beyond its melting point (62 °C).

2.4.4 Silicone

The silicone rubber's contribution to the overall stiffness of the composite beams is minimal in comparison to the rigid smart materials, but its stiffness is analyzed experimentally nevertheless for the sake of improved accuracy. Figure 2.6(d) shows the load-deflection data from measurements taken at all 7 testing temperatures; the silicone's behavior is nearly identical at each of the temperatures.

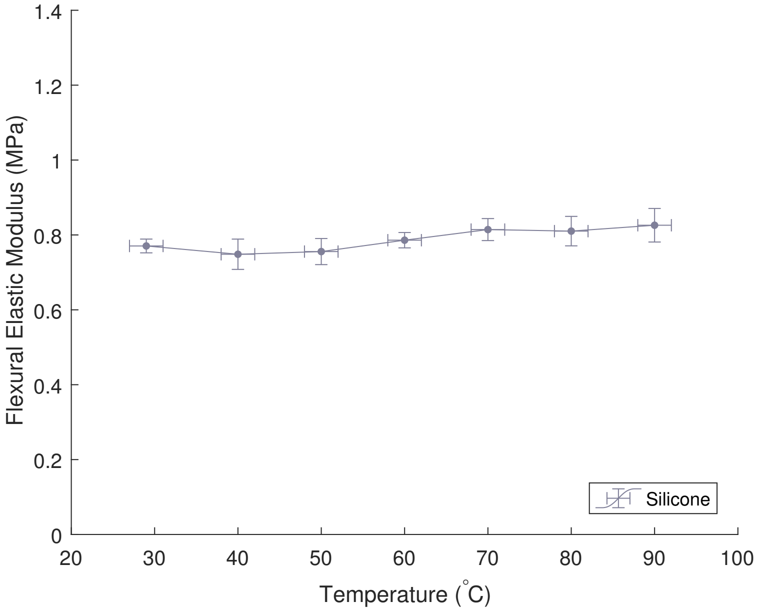

Figure 2.10 Measured flexural elastic modulus of pure silicone rubber as a function of temperature. The modulus values were obtained using the slopes of the load-deflection curves in Figure 2.6(d).

The silicone serves primarily as a matrix for combining smart materials and does not exhibit smart behavior itself. In other words, the material properties of the silicone are not expected to change significantly with temperature. This lack of temperature-dependence in the stiffness is also evidenced by the plot in Figure 2.10 which shows nearly constant elastic modulus across the range of temperatures.

2.4.5 PCL/Nitinol composite

The smart composite consisting of Nitinol and PCL rods in the silicone matrix offers desirable stiffness variability. The PCL rod provides high stiffness at low temperatures while the Nitinol rod exhibits high stiffness at high temperatures. At mid-range temperatures, both materials provide minimal rigidity to the composite, causing very low stiffness at temperatures around 40 to 50 °C. The beam stiffness is characterized by its flexural elastic modulus calculated from the slopes of the load-deflection curves from Figure 2.6(e).

As seen in Figures 2.1 and 2.11, three discrete stiffness levels are observed between temperatures of 29 and 90 °C. This unique stiffness variation across the range of temperatures is due to the smart behavior of its constituent materials. Theoretically, the sum of the loads incurred by the pure PCL, Nitinol, and silicone should match the measured load of the composite beam at any temperature. The modulus values in Figure 2.11(a) and (b) were all calculated from Equation 2.1 using the geometric dimensions of the silicone for w and h. Since the values of w and h were the same for each sample, the modulus of the PCL/Nitinol composite should line up with the sum of the moduli of the constituent materials. The shape of the curve in Figure 2.11(a) does indeed match nearly identically the summation of the modulus curves for the constituent materials in Figure 2.11(b).

The highest stiffness for the PCL/Nitinol composite beam is achieved at temperatures below about 30 °C, where the Nitinol is martensitic and the PCL remains solid. The modulus in at 29 °C reaches up to 7.8 ± 0.3 MPa. The stiffness reaches a minimum of 3.3 ± 0.8 MPa around 50 °C when the composite becomes flexible as the PCL melts. The Nitinol remains martensitic in this region, allowing large deformation as the microstructure transforms from twinned to de-twinned martensite. The medium stiffness range occurs between 70 and 90 °C with an average modulus of 7.1 ± 0.1 MPa where the PCL is melted but the Nitinol transforms to austenite.

A unique twisting behavior was observed in the testing of the PCL/Nitinol composite

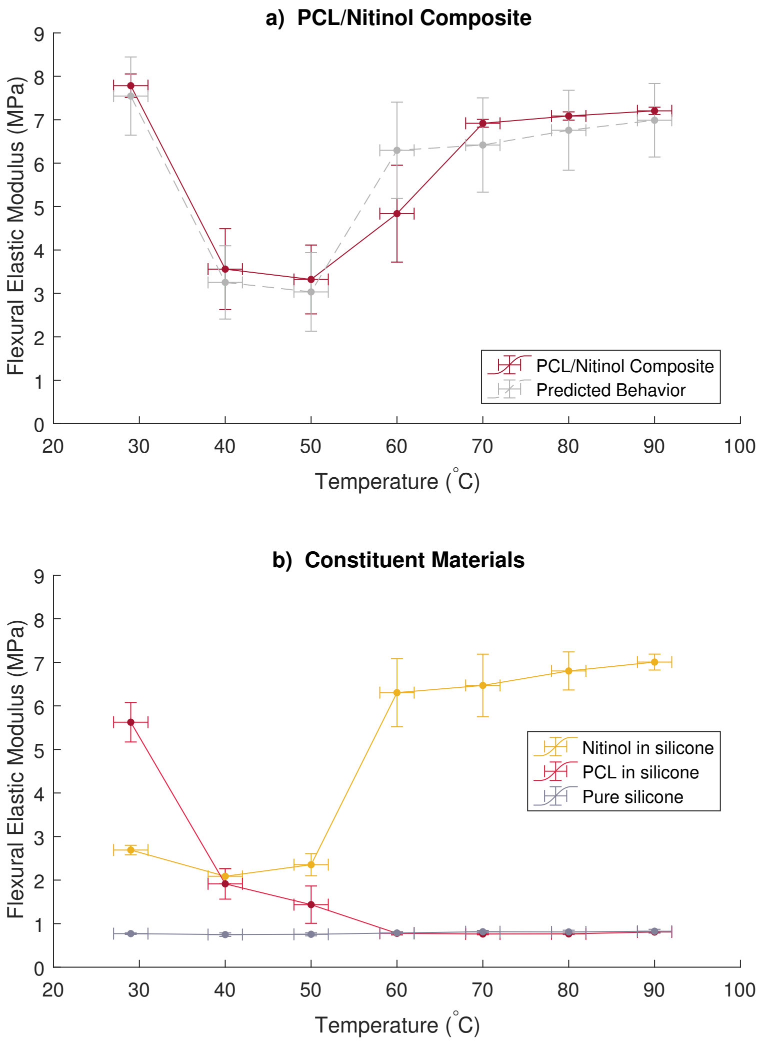

Figure 2.11 Measured flexural elastic modulus of PCL/Nitinol Composite and constituent materials as a function of temperature. The dashed gray curve in (a) shows the predicted modulus of the composite based on the sum of the individual material moduli.

above 60 °C;, the composite twisted under the applied load of the bend test. At low temperatures, the parallel rods resist torsion, but above 60 °C, the PCL melts and provides no resistance to torsion in the composite beam. When applied to bulk materials, this feature could provide directional stability upon localized melting of specific PCL members.

2.4.6 Field's metal/Nitinol composite

The combination of the smart behavior of Nitinol and Field's metal in the silicone rubber matrix results in a composite beam with unique, temperature-dependent properties. The Nitinol again provides the composite with high stiffness at high temperatures. Similar to the PCL, the Field's metal also offers high stiffness at low temperatures, but the Field's metal melts at a higher temperature than the PCL. Because the Field's metal has a higher melting point than the PCL, the 3 distinct stiffness regions are not distinguishable in Figures 2.2 and 2.12(a). The reason for this indistinct stiffness region at mid-range temperatures is explained by the behavior of the constituent materials shown in Figure 2.12(b). As the Field's metal begins to soften and melt, the Nitinol simultaneously transitions to austenite which counteracts the stiffness change of the Field's metal as it melts. In the case of the PCL/Nitinol composite, the PCL melted before the Nitinol began its phase transformation, which resulted in a low stiffness region at mid-range temperatures. For the Field's metal/Nitinol composite, however, the smart behavior of the constituent materials is activated at roughly the same temperature, so only 2 distinct stiffness regions are visible in Figures 2.2 and 2.12(a).

At room temperature (29 °C), the combination of the martensitic Nitinol and solid Field's metal produces a stiffness of 19.0 ± 0.8 MPa. As the composite is heated, the Field's metal begins to soften and weaken the beam while the Nitinol begins simultaneously transforming to austenite, causing a gradual decline in stiffness. The composite reaches a minimum modulus of 6.4 ± 0.1 MPa at 70 °C. Beyond this point, the Field's metal remains melted and the Nitinol is completely austenitic, so the stiffness platteaus and remains relatively constant with further heating.

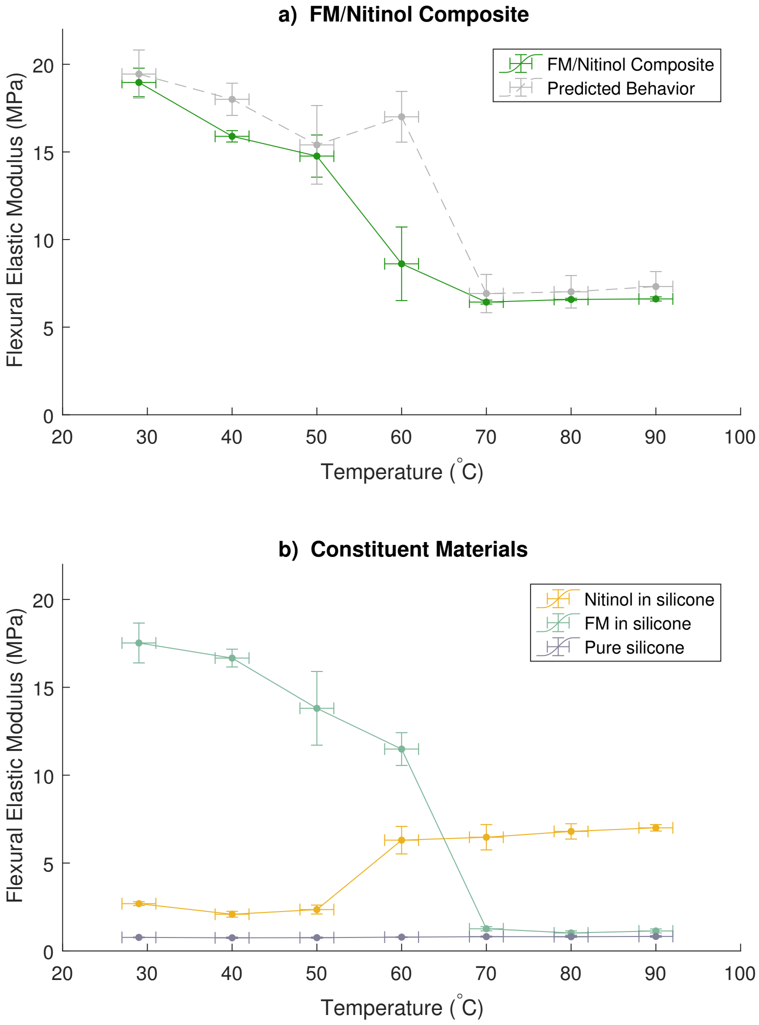

Figure 2.12 Measured flexural elastic modulus of FM/Nitinol Composite and constituent materials as a function of temperature. The dashed gray curve in (a) shows the predicted modulus of the composite based on the sum of the individual material moduli.

Table 2.2 Joint temperatures for 9 configurations achieved by 2-joint PCL/Nitinol composite finger actuated by the same 20N tendon force. Note that configurations g, h, and i are mirrored versions of the configurations marked with an *.

	Distal Joint		Proximal Joint		
Configuration	Temp	Stiffness	Temp	Stiffness	Tendon Force
a	29 °C	high	29 °C	high	20N
b*	29 °C	high	45 °C	low	20N
c*	90 °C	medium	29 °C	high	20N
d	45 °C	low	45 °C	low	20N
e*	90 °C	medium	45 °C	low	20N
f	90 °C	medium	90 °C	medium	20N
g	45 °C	low	29 °C	high	20N
h	29 °C	high	90 °C	medium	20N
i	45 °C	low	90 °C	medium	20N

2.4.7 Smart composite finger

As shown in Figure 2.13, the PCL/Nitinol composite finger proved capable of forming 6 different configurations with a single tendon tensioned at 20N. The PCL/Nitinol composite bend test results from Figure 2.11(a) showed that the composite can exhibit 3 different stiffness levels between 29 and 90 °C: high stiffness at low temperatures, low stiffness at mid-range temperatures, and medium-high stiffness at high temperatures. By heating the finger joints to various combinations of temperatures in different stiffness regions, the shape of the finger can be precisely controlled. Table 2.2 shows the joint temperatures for all 9 configurations possible with a 20N tendon force. Configurations g, h, and i are not shown in Figure 2.13 because they are simply mirrored versions of configurations b, c, and e.

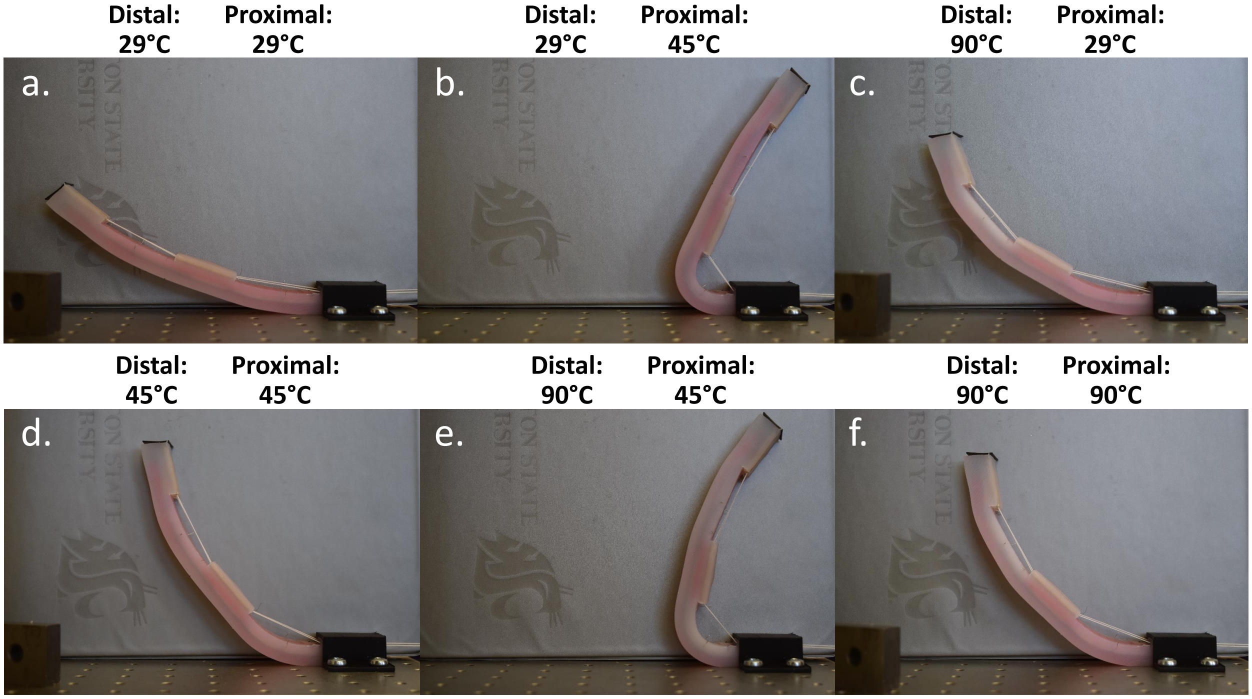

Figure 2.13 Six different finger configurations achieved with a single tendon. Different combinations of joint temperatures enabled 6 different configurations with the application of the same 20N tendon force in each scenario.

2.5 Discussion

Ultimately, the PCL/Nitinol composite exhibited 3 different stiffness levels at temperatures between 29 and 90 °C, and the Field's metal/Nitinol composite showed a jump between two stiffness levels at about 60 °C. Due to the smart behavior of the constituent materials, these different stiffness levels may be activated with a simple temperature stimulus. In this experiment, a thin resistance wire was used to supply Joule heating to the composites, but other heating methods could be used that may offer more uniform heating. Methods for heat dispersion should also be explored as cycling time is a concern among most shape memory alloys and other thermally activated systems.

In order to develop an effective system for controlling composite smart materials, it is necessary to develop an accurate model for the composite beam stiffness. Due to the smart behavior of each component and their inelastic behavior under large loads, the composite beam stiffness is a complicated function of both temperature and applied load. The recoverable strain limit is a factor that limits the usability of smart material composites for robotics applications. The PCL and Field's metal can endure unlimited strain because they may be melted and re-solidified to reset any permanent deformation. Thus, the composite stiffness relies on not only the current strain, but also on the configuration at which the PCL or Field's metal was last allowed to solidify. The shape memory effect of the Nitinol allows it to recover from any deformation up to 7% strain when heated above its transformation temperature. However, when the Nitinol is austenitic, deformation beyond the elastic limit is unrecoverable and thus limits the load the composite is capable of exerting.

The melting and re-solidifying of the low melting temperature materials (PCL and Field's metal) further complicates the model, but these factors should be encompassed in order to develop a model that characterizes the behavior of the two composite beams under all temperatures and applied loads.

In this experiment, tests were conducted on composite beams comprised of rods with one specific size and shape. However, customization of the stiffness in each temperature region may be achieved by modifying the geometry of the individual rods. This will alter the bending inertia of the individual materials and allow the magnitude of each discrete stiffness region to be customized to suit the relevant application. The temperature stimuli can also be shifted slightly by changing material compositions and alloying elements. For example, the Field's metal/Nitinol composite only showed two stiffness regions because the critical temperature of the Nitinol was too close to the melting point of the Field's metal to allow an intermediate stiffness region. However, by slightly altering the alloy composition of the Field's metal, the melting point can be easily adjusted. There also exist other low melting point materials that may be useful for incorporating in smart composite robotics.

The PCL/Nitinol composite exhibited three different stiffness regions as anticipated. However, the high stiffness and medium stiffness levels were very similar, almost to the extent that the high-low-medium stiffness sequence might be considered a high-low-high sequence. Depending on the application, a more diverse range of stiffness levels may be desired. The relative stiffness levels can be easily tuned by simply altering the thickness ratio of the smart materials used. For example, by using a thinner Nitinol rod without changing the dimensions of the PCL, the composite would exhibit a more distinct medium stiffness level at high temperatures.

2.6 Summary of Results

Composite beam samples were constructed with combinations of PCL/Nitinol and Field's metal/Nitinol rods positioned in parallel within a silicone matrix. The resulting composite stiffness was evidenced through 3-point bend tests conducted on the composite beams and their constituent materials at 7 different temperatures between 29 and 90 °C. Three discrete stiffness levels were observed in the behavior of the PCL/Nitinol composite beams. Twisting behavior was also observed in the case of the PCL/Nitinol composite as the PCL melted and allowed rotation about the Nitinol rod. The Field's metal/Nitinol composite beam exhibited only two. stiffness levels between 29 and 90 °C because the melting of the Field's metal and the phase transformation of the Nitinol ocurred at nearly the same temperature. Heating of the PCL/Nitinol composite resulted in a high, low, medium stiffness sequence. The Field's metal/Nitinol composite exhibited high stiffness at low temperatures and lower stiffness at higher temperatures. By including different smart materials and modifying the relative thicknesses of the constituent materials, the stiffness levels and temperature ranges can be finely tuned to suit a variety of applications.

Characterizing the stiffness as a function of temperature for composite smart materials and their constituent materials is a substantial step toward developing adept soft robotic materials. From these results, a visible correlation was found between the composite stiffness and the stiffness of each constituent material at any given temperature. Thus, by selecting appropriate smart materials, smart composites with numerous stiffness levels at different temperatures may be designed, and the stiffness of the resulting composites may be predicted through a simple weighted summation of the component stiffnesses.

As demonstrated by the smart composite finger, compositing multiple smart materials in parallel within a robotic member could enable highly dexterous manipulation with minimal complexity. Six different configurations were achieved with single tendon by selectively heating the joints to activate different stiffness levels. By including more smart materials, more stiffness levels could be achieved, enabling more precise control.

Applications for smart composite materials extend beyond the realm of simple robotic fingers to meet design requirements in applicaions ranging from wearable devices to co-robotic environments and in-home health care. Further research will explore the effects of extending these smart material composites into 3 dimensions and thereby enabling highly intelligent manipulation.

Chapter Three

GEOMETRIC DESIGN AND CONTROL

Attribution:

This chapter is a modification of two original papers previously published.

Contributions from:

John P. Swensen[1], Brandon C. Townsend[1]

[1]School of Mechanical and Materials Engineering, Washington State University, Pullman, WA

This text is published with the following citations:

E. A. Allen and J. P. Swensen, “Directional stiffness control throughgeometric patterning and localized heating of fields metal latticeembedded in silicone,” *Actuators*, vol. 7, no. 4, p. 80, nov 2018.

E. A. Allen, B. C. Townsend, and J. P. Swensen, “Configuration Modeling of a Soft Robotic Element with Selectable Bending Axes,” in Proc. *IEEE/RSJ International Conference on Intelligent Robots and Systems (IROS2019)*, Macau, China, Nov. 2019.

3.1 Abstract

This paper presents an approach for modeling new soft robotic materials which possess the ability to control directional stiffness. These materials are inspired by biological systems where movements are enabled by variable stiffness tissue and contraction of localized muscle

groups. Here a low-melting-point (LMP) material lattice embedded in an elastomer serves as a rigid skeleton that may be locally melted to allow bending at selectable joint locations. The forward kinematics of the lattice is modeled using the product of exponentials method with the incorporation of bending axis selectivity. We then develop this model to account for torques imposed by tendons, and we model the elastomer's resistance to bending as a torsional spring at the selected joints. Thus we obtain a two-way relationship between tendon forces and joint angles/axes. The concept of applying traditional robot modeling strategies to selectively compliant robotic structures could enable precise control of dexterous soft robots that satisfy stringent safety criteria.

3.2 Introduction

Several novel approaches to soft robotics actuation have been innovated in the last several years as researchers explore the soft robotics alternative to traditional rigid robots. With the growing demand for at-home healthcare and the push for industrial co-robots, safety and adaptability are a high priority for modern robots [2]. The intrinsically soft nature of the soft robotics approach offers solutions to safety concerns and shows great promise for mimicking human abilities [3, 24, 86]. Unlike traditional robots, soft robots can deform upon impact to prevent injuries. Several approaches have been developed to address the strength/flexibility trade-off introduced by the soft robotics approach [2, 87].

In an effort to maintain the structural integrity of traditional robots, variable stiffness actuators operate by varying the stiffness transmitted to joints between rigid links. Antagonistic arrangements of actuators mimic human muscle configuration and can exhibit a nonlinear relationship between input torque and angular joint deflection [59–61]. Other methods use advanced control systems to enable variable stiffness. Although these methods offer high-level precision and reliability, their practicality is limited by size, weight and bandwidth, and they are generally not suitable for material actuators with multiple degrees of freedom [27, 62].

Variable stiffness structures are comprised of prestressed struts and cables that hold the structure in a configuration; by selectively releasing and re-tensioning cables within a robotic system, a variety of predictable motions may be activated [63, 64, 66]. Similarly, the application of 4D printing to soft robotics has enabled assemblies that self-bend when exposed to light, heat, electricity, or other means of stimulation. A patterned ink deposition causes heating/shrinkage at folding sites or localized swelling of media within polymer matrices under infrared exposure [88, 89]. Other researchers have designed robotic structures using origami techniques [77]. Soft robotic actuators for specific applications are often designed to meet the compliance requirements of the system at hand [24]. Many soft actuators are fabricated with geometrically patterned pneumatic chambers that deform the elastomer when pressurized [12, 67, 68, 90, 91]. Although elastomers are inherently weak, fiber reinforcement and high pressure supplies offer high strength capabilities [86, 92, 93].

Research similar to the work in this paper is driven by a need for soft robotic structures/materials that can exhibit both high strength and compliant behavior. The impressive capabilities of biological systems such as muscular hydrostats and catch-connective tissue inspire the design of soft robotic materials whose stiffness can be precisely controlled [54, 55]. Some researchers have explored the use of low-melting-point (LMP) materials to enable stiffness variability [45, 51, 78, 79, 94, 95]. Heating of these materials causes the internal skeleton to melt and allow compliant behavior when desired.

These concepts are expanded to enable directional stiffness control by locally melting the skeleton at designated locations. In this work, we propose a method for modeling the configuration of an element with selectable bending axes.

A 3-link soft robotic element has been proposed with an internal rigid skeleton that may be selectively melted to allow bending about specified axes as shown in Figure 3.1. The element consists of a low-melting-point (LMP) metal or polymer lattice encased in silicone rubber with nichrome heating elements arranged to allow selection of bending axes.

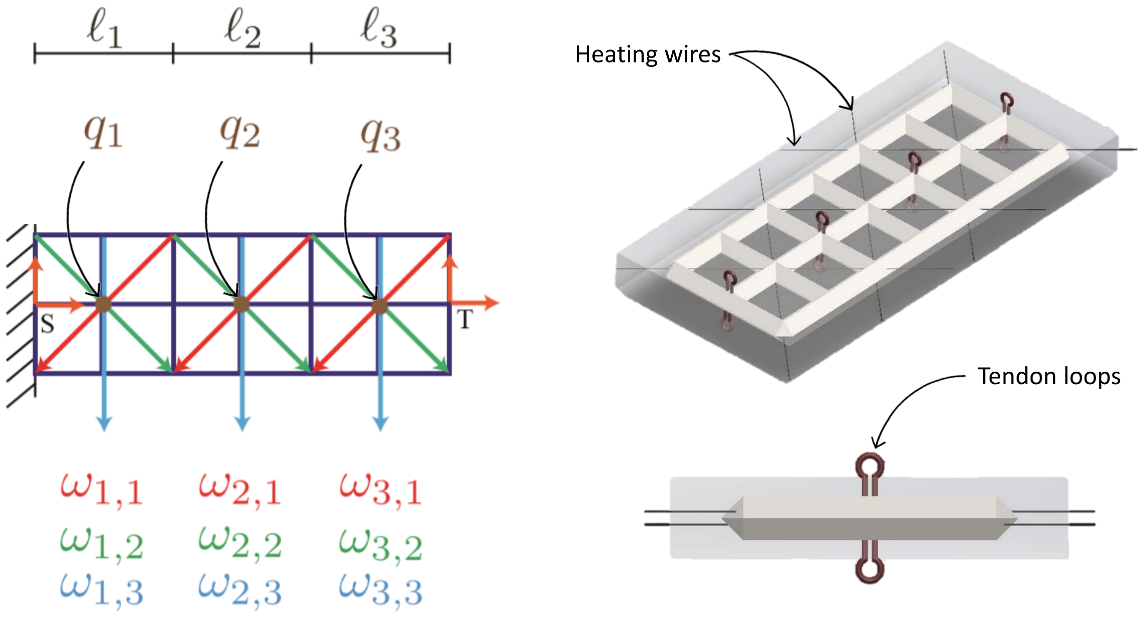

Figure 3.1 Design of 3-link soft robotic element with internal LMP lattice that can be selectively melted to allow bending about 9 different axes. The colored arrows represent the 9 selectable bending axes denoted by $\omega_{i,j}$, where i refers to the segment number and j is the axis direction. The points q_1, q_2, and q_3 lie at the centers of the 3 segments.

The nine selectable bending axes represented by $\omega_{i,j}$, are shown in Figure 3.1, where i refers to the segment number and j is the axis direction. For this problem, up to 3 of the 9 bending axes may be selected at once (up to one axis per segment) by localized melting of the lattice. As shown in Figure 3.2, a tendon is attached to each side of the element to induce bending about the selected compliant axes. The forward kinematics of this element are constructed using the product of exponentials method to determine the configuration based on the selected axes and corresponding joint angles. A variety of unique configurations may be achieved as shown in Figure 3.3 with minimal complexity.

For this paper, we derive the forward kinematics relationships, then take this model a step further by relating applied tendon forces to the deformation of the piece. This involves modeling the joints (melted axes) as torsional springs with some constant stiffness. By

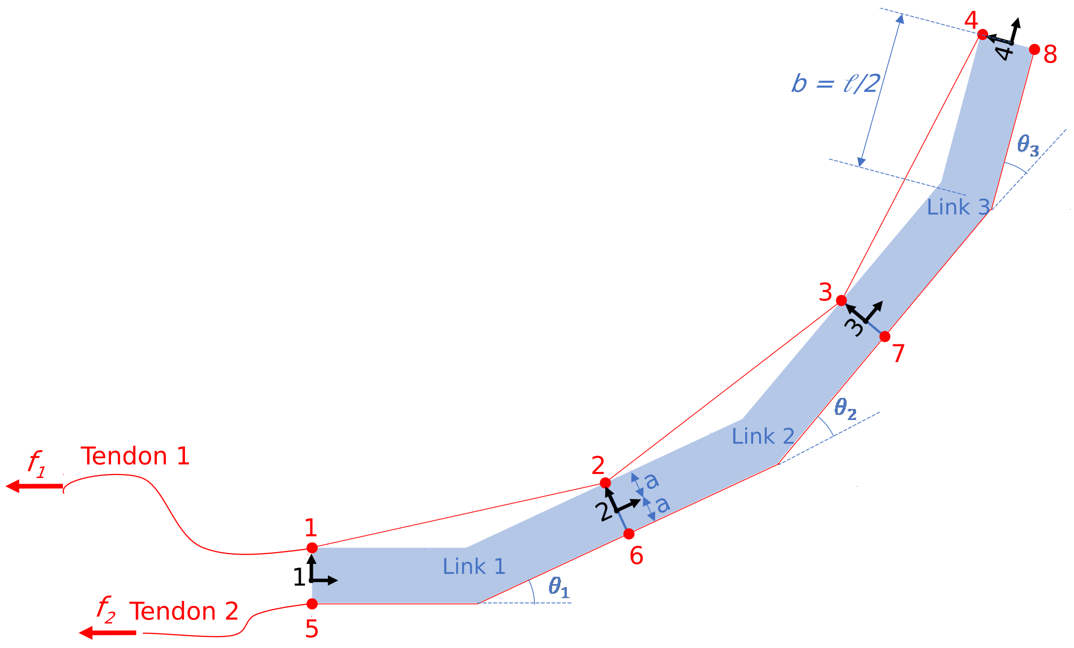

Figure 3.2 Planar view of tendon routing for 3-link soft robotic element when the 3 transverse axes are melted simultaneously.

relating tendon forces to the element's configuration, we may determine what configurations are possible for any given axis selection.

Each set of equations is derived as a function of ω, the set of selected axes which may include a single axis or up to 3 of the 9 possible bending axes. Each time that a segment is deformed and then cooled, the reference configuration of the model changes and must be updated. By successively melting different joints and controlling tendon forces, a vast range of configurations may be achieved by this simple element.

Successive melting drastically improves the work space of the device, allowing for finer control using only a single tendon. When individual joints may be selected to melt on their own, or even in pairs rather than all three, the shape of the device may be more precisely controlled. Simultaneous melting only allows for the bending of all selected joints at once, with each joint experiencing approximately the same angular displacement. This provides both little control and limited workspace. Selective melting allows for configurations and tool tip positions that would not otherwise be achievable by allowing for the manipulation

Figure 3.3 A few unique configurations achievable through selective melting and deformation of soft robotic element.

of individual joints while the other joints remain fixed.

3.3 Materials and Methods

3.3.1 Test Piece Fabrication

A test piece consisting of an LMP Field's metal (FM) lattice encased in a thin silicone matrix is fabricated to demonstrate the directional stiffness controllability that can be achieved through localized heating. Figure 3.4 shows the step-by-step fabrication process for the test piece. First, a mold is 3D printed out of Polyvinyl alcohol (PVA) following fabrication methods proposed by Swensen et al. [96] with hollow, diamond-shaped channels inside for the FM. The diamond shape of the channels eliminates the need for printing support material in the mold. An injection hole and tiny vent holes are drilled in the top of the mold after printing to allow air to escape as the FM is injected with a syringe. After the metal solidifies in the channels, the mold is submerged in water for two days until the PVA mold is completely dissolved, exposing the bare FM lattice. The silicone matrix is then cast in layers to ensure proper spacing between components and prevent direct contact between the Nichrome heating elements and the FM lattice. A similar method is employed to encapsulate an LMP plastic (PCL) lattice in silicone, except the PCL filament can be directly 3D printed into the desired lattice shape and does not require a soluble die.

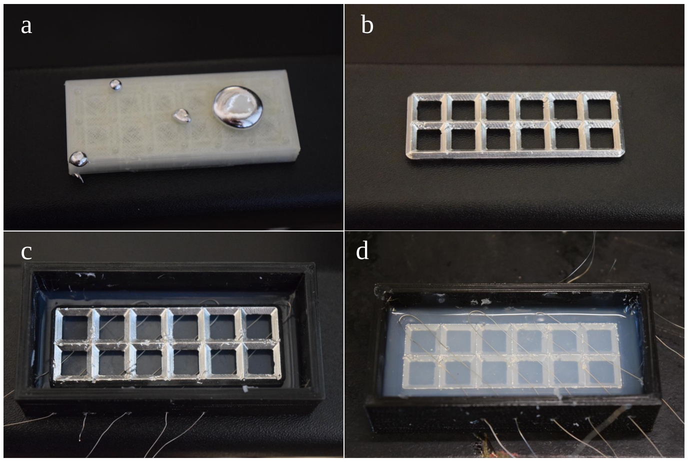

Figure 3.4 The fabrication steps for patterned FM test piece, showing (**a**) FM injected into the 3D-printed soluble mold, (**b**) FM lattice with soluble mold material dissolved, (**c**) layout of Nichrome heating elements, and (**d**) final casting layer of silicone matrix.

3.3.2 Deriving Forward Kinematics with Changing Axes of Compliance

Using the language of differential geometry represented as Lie groups and Lie algebras [97], rigid body transforms between coordinate frames are often represented in terms of the exponential map from the Lie algebra $SE(3)$ to the Lie group $SE(3)$. In the general case, given a function of instantaneous velocities represented as the screw $\hat{\xi}(t) \in SE(3)$, with $\hat{}: R^6 \to SE(3)$ the isomorphism between the reals and the Lie algebra, the relationship between the instantaneous velocities and the corresponding coordinate frame transformation is

$$g_{ab}(t) = e^{\int_0^t \xi_\tau d\tau} g_{ab}(0), \;\; g_{ab}(t) \in SE(3). \tag{3.1}$$

In the particular case where the instantaneous velocities can be written as the product of a constant twist and a time-varying parameter, $\hat{\xi}(t) = \hat{\xi}_c q(t)$, the treatment of $g_{ab}(t)$ and its time derivatives are greatly simplified. The tunably compliant FM test piece here is explicitly designed such that constant twists describe its motion in each of the tunably compliant configurations. This behavior is observable in Figure 3.5 where its bending along each of the axes can be described by a constant twist multiplied by a bend angle. Then, the serial chain of tunably compliant axes may be described as a product of exponentials where the direction of compliance of each segment is parameterized by an associated constant twist and joint motions,

$$g_{ST}(q) = e^{\xi_1 q_1(t)} e^{\xi_2 q_2(t)} \ldots e^{\xi_n q_n(t)} g_{ST}(0). \tag{3.2}$$

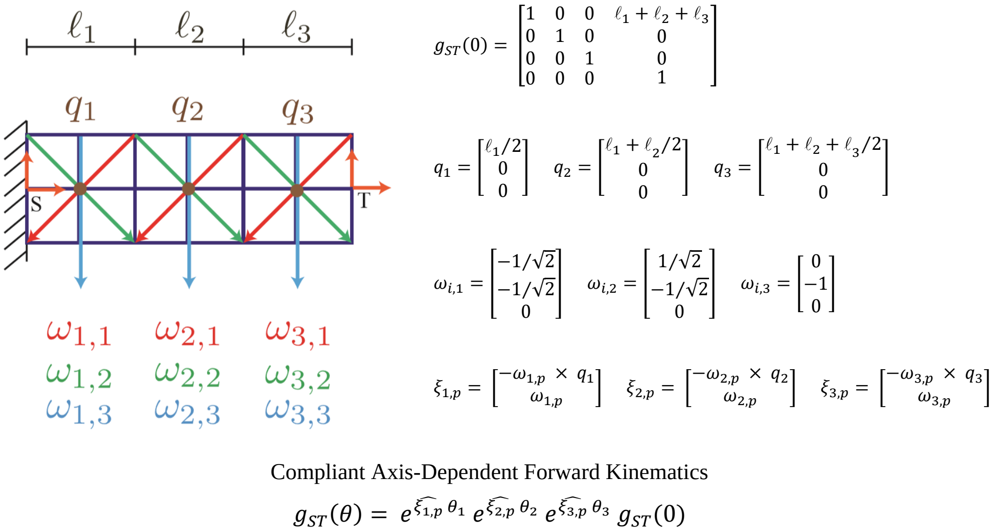

Figure 3.5 The kinematics of 3-segment lattice where the axes of compliance can be chosen through selective melting. Here the kinematics are developed using a product of exponentials formulation and the axis of rotation is defined by the axis of selective melting for each segment, $w_{i,p}$. These potential axes of compliance are shown for each segment in red, green, and blue.

This type of kinematic simplification is demonstrated in Figure 3.5 for a 3-segment case of the LMP truss fabricated for this experiment. In this example, two heaters in each segment allow the truss to be melted along either diagonal axis, $w_{i,1}$ or $w_{i,2}$, or when both are heated simultaneously the axis of rotation is $w_{i,3}$. The elastomer elements surrounding the low-melting-point metals can be modeled as a torsional spring about the axis of compliance cause by the melted metal. This approach relies on mechanism simplifications for compliant mechanism pioneered by Howell [98], where compliant joints are considered using pseudo-rigid body modeling with joints that are not fixed. Thus, the tendon force to mechanism configuration can be solved through a combination of the forward kinematics, associated Jacobian, and the tendon routing and tension force. As shown in Figure 3.5, the axis directions $w_{i,i}$, a point that lies on the selected axis q_i, and the reference configuration $g_{ST}(0)$ (defined where all joint angles are zero) are used to develop the compliant axis-dependent forward kinematics of the system.

$$\xi_{1,3} = \begin{bmatrix} 0 \\ 0 \\ -\ell_1/2 \\ 0 \\ -1 \\ 0 \end{bmatrix} \qquad \xi_{2,3} = \begin{bmatrix} 0 \\ 0 \\ -\ell_1 - \ell_2/2 \\ 0 \\ -1 \\ 0 \end{bmatrix} \qquad \xi_{3,3} = \begin{bmatrix} 0 \\ 0 \\ -\ell_1 - \ell_2 - \ell_3/2 \\ 0 \\ -1 \\ 0 \end{bmatrix}$$

$$\widehat{\xi_{3,3}} = \begin{bmatrix} 0 & 0 & -1 & 0 \\ 0 & 0 & 0 & 0 \\ 1 & 0 & 0 & -\ell_1/2 \\ 0 & 0 & 0 & 1 \end{bmatrix} \quad \widehat{\xi_{2,3}} = \begin{bmatrix} 0 & 0 & -1 & 0 \\ 0 & 0 & 0 & 0 \\ 1 & 0 & 0 & -\ell_1 - \ell_2/2 \\ 0 & 0 & 0 & 1 \end{bmatrix} \quad \widehat{\xi_{3,3}} = \begin{bmatrix} 0 & 0 & -1 & 0 \\ 0 & 0 & 0 & 0 \\ 1 & 0 & 0 & -\ell_1 - \ell_2 - \ell_3/2 \\ 0 & 0 & 0 & 1 \end{bmatrix}$$

Forward Kinematics for Specific Selection of Compliance Axes $\omega_{1,3}$, $\omega_{2,3}$, $\omega_{3.3}$

$$g_{ST}(\theta) = \left(e^{\begin{bmatrix} 0 & 0 & -1 & 0 \\ 0 & 0 & 0 & 0 \\ 1 & 0 & 0 & -\frac{\ell_1}{2} \\ 0 & 0 & 0 & 1 \end{bmatrix}\theta_1} \right) \left(e^{\begin{bmatrix} 0 & 0 & -1 & 0 \\ 0 & 0 & 0 & 0 \\ 1 & 0 & 0 & -\ell_1-\frac{\ell_2}{2} \\ 0 & 0 & 0 & 1 \end{bmatrix}\theta_2} \right) \left(e^{\begin{bmatrix} 0 & 0 & -1 & 0 \\ 0 & 0 & 0 & 0 \\ 1 & 0 & 0 & -\ell_1-\ell_2-\frac{\ell_3}{2} \\ 0 & 0 & 0 & 1 \end{bmatrix}\theta_3} \right) \begin{bmatrix} 1 & 0 & 0 & \ell_1 + \ell_2 + \ell_3 \\ 0 & 1 & 0 & 0 \\ 0 & 0 & 1 & 0 \\ 0 & 0 & 0 & 1 \end{bmatrix}$$

Figure 3.6 Development of forward kinematics matrices for specific example case where compliance axes $\omega_{1,3}$, $\omega_{2,3}$, and $\omega_{3,3}$ are selected, allowing bending along the three transverse axes.

The forward kinematics matrices for an example case are shown in Figure 3.6 where the compliance axes $\omega_{1,3}$, $\omega_{2,3}$, and $\omega_{3,3}$ are selected.

3.3.3 Shape Predictive Model

A predictive model of the lattice bending is constructed based on the product of exponentials method to describe the bending of the structure as different elements are heated. By placing reference coordinate frames at intermediate points along the lattice, the coordinates of each of the 21 lattice vertices can be calculated given bending axis selections and joint angles as inputs. Points on the lattice between the base and the first axis $w_{1,i}$ are not affected by any joint bending; lattice points between $w_{1,i}$ and $w_{2,i}$ are affected only by the axis and angle of the first joint; lattice points between $w_{2,i}$ and $w_{3,i}$ are affected by the first two joints; and lattice points beyond the third joint are affected by the axis and bending angle of every joint. Placing a reference coordinate frame at the center q_i of each of the three segments that rotates and shifts with the lattice based on the bending of the preceding joints simplifies the modeling of points on the lattice. Each of these intermediate coordinate frames has its own reference configuration ($g_{SU}(0)$, $g_{SV}(0)$, $g_{SW}(0)$) which is multiplied by the matrix exponentials of only the joints that precede it. As shown in Figure 3.5, the forward kinematics equation $g_{ST}(\theta)$ relating configuration of the tool frame relative to the stationary frame relies on the product of exponentials from all three joints. The kinematics equations relating the intermediate frames to the stationary frames rely on only the exponentials for the joints that exist between the two frames being related. This model can then be used to plot the shape of the element for any input joint angles and axis selection.

3.3.4 Extension Functions for Tendons

The torque applied on the joints by the tendons depends on the tendon routing configuration and the axes that have been selected. For example, if the tendon does not lie perpendicular to the selected bending axis, a larger tendon force will be required to achieve the same torque about the joint. These geometric relationships between tendon force and joint torque are derived as a function of each possible axis selection ω, joint angle θ, and tendon offset a.

The joint torques τ may be directly related to the tendon forces by developing extension functions for each tendon. This method of analyzing inelastic tendons is described by Murray et al. [97]. This method involves deriving the extension function for each tendon, which expresses the length of the tendon as a function of the joint angles. In our case, since the axis directions may vary, the extension functions depend on both the joint angles and the selected axes.

For a simple planar problem, developing these extension functions may be done by simply analyzing the geometry. For example, if the axes $\omega_{1,3}, \omega_{2,3}$, and $\omega_{3,3}$ (transverse axes), are selected, the geometric relationships may be extracted by inspection of the planar diagram in Figure 3.2. However, when different axes are selected, the problem is no longer planar, and these geometric relations become nontrivial.

Rather than developing complicated, three-dimensional geometric relationships for each bending axis combination, the forward kinematics exponential may be used to express the length of each tendon for any set of selected axes and joint angles. The length of tendon 1, as shown in Figure 3.2, is simply the sum of the distances between tendon fixation points 1 and 2, 2 and 3, 3 and 4. These distances are already known from the forward kinematics for this element developed above which yield

$$x_{1,1}(\theta_1, \omega_1) = \begin{bmatrix} 0 & 0 & a & 1 \end{bmatrix}^\top, \tag{3.3}$$

$$x_{2,1}(\theta_1, \omega_1) = e^{\widehat{\xi_1(\omega_1)}\theta_1} g_{1,2_0} \begin{bmatrix} 0 & 0 & a & 1 \end{bmatrix}^\top, \tag{3.4}$$

where $\xi_1(\omega_1)$ is the twist used to represent the rotation and translation of points due to bending about the selected axis ω_1. Here the second subscript indicates the frame of reference, so $x_{2,1}$ represents the homogeneous coordinates of point 2 relative to frame 1. The matrix exponential $e^{\hat{\xi}_1 \theta_1}$ used to transform points from frame 1 to 2 has been previously developed as a function of ω in the construction of the forward kinematics relationships for this element. The reference configuration $g_{1,2_0}$ is the transformation between frames 1 and 2 when $\theta_1 = 0$. For this case,

$$g_{1,2_0} = \begin{bmatrix} 1 & 0 & 0 & \ell_1 \\ 0 & 1 & 0 & 0 \\ 0 & 0 & 1 & 0 \\ 0 & 0 & 0 & 1 \end{bmatrix}, \tag{3.5}$$

where ℓ_1 is the length of link 1. The distance between $x_{1,1}$ and $x_{2,1}$ may then be computed as:

$$d_{1-2}(\theta_1, \omega_1) = \sqrt{(x_{1,1}^\top x_{1,1})^2 + (x_{2,1}^\top x_{2,1})^2}. \tag{3.6}$$

Finally, when the joint angles are all positive, the extension function for tendon 1 may then be computed by summing the distances between each tendon fixation point:

$$h_1(\theta, \omega) = d_{1-2} + d_{2-3} + d_{3-4}, \tag{3.7}$$

where d_{2-3} and d_{3-4} are computed using the matrix exponential for rotation about ω_2 and ω_3. The extension function for tendon 2 may simply be expressed as

$$h_2(\theta, \omega) = \ell_1 + a\theta_1 + \ell_2 + a\theta_2 + \ell_3 + a\theta_3 \tag{3.8}$$

when the joint angles are all positive. In theory, there are 8 different cases for these extension functions based on different combinations of positive and negative joint angles. For example, if θ_1 and θ_2 are positive while θ_3 is negative, the extension functions would behave differently than if all the joint angles were positive. Thus, extension functions are different for each of the 8 cases of positive/negative joint angle combinations. However, for this project we only have two tendons, so if we consider only simultaneous melting, the only possible joint angle combinations are case 1 (all joint angles are positive) and case 8 (all joint angles are negative). For case 8, the joint angles are all negative (i.e. tendon 2 is activated instead of tendon 1), and the extension functions are reversed as follows:

$$h_1(\theta, \omega) = \ell_1 - a\theta_1 + \ell_2 - a\theta_2 + \ell_3 - a\theta_3, \tag{3.9}$$

$$h_2(\theta, \omega) = d_{5-6} + d_{6-7} + d_{7-8}. \tag{3.10}$$

3.3.5 Coupling Matrix

According to Murray et al. [97], by applying the conservation of energy, the joint torques can be expressed as

$$\tau = P(\theta, \omega) f = P(\theta, \omega) \begin{bmatrix} f_1 & f_2 \end{bmatrix}^\top, \tag{3.11}$$

where f is a vector containing the forces on each tendon, and where $P(\theta, \omega)$ is the coupling matrix computed from

$$P(\theta, \omega) = \frac{\partial h^\top(\theta, \omega)}{\partial \theta}. \tag{3.12}$$

Here h is a vector containing the extension functions for the appropriate case of positive/negative joint angle combinations:

$$h(\theta,\omega) = \begin{bmatrix} h_1(\theta,\omega) & h_2(\theta,\omega) \end{bmatrix}^\top . \tag{3.13}$$

The computation of $P(\theta,\omega)$ is non-trivial. Since the extension functions h depend on the joint angles and selected axes, and they involve matrix exponentials and square roots, taking the derivatives for $P(\theta,\omega)$ by hand would be tedious and nearly impossible. The extension functions for all 8 cases were entered into Mathematica for the analytical computation of these derivatives. The resulting coupling matrix for each case, expressed as a function of $\theta, \omega, a, \ell_1, \ell_2$, and ℓ_3, was then converted to MATLAB using the "ToMatlab" package.

3.3.6 Measuring Joint Stiffnesses

The joint stiffness modeled by the torsional springs is dependent on the geometry of the element at the joint and the material properties of the elastomer. By assuming Hooke's Law behavior, the torque exerted by a single spring (joint) can be expressed as

$$\tau = k\theta, \tag{3.14}$$

where θ is the resulting joint angle relative to the equilibrium configuration, and k is the spring constant which may be determined experimentally. k depends on the elastic modulus of the material and the area moment of inertia of the joint cross-section.

For this particular project, there are only two different cross-sections for the nine different allowable bending axes: a cross-section for the straight (transverse) axes, and a slightly wider cross-section for the diagonal axes. A primitive experiment setup shown in Figure 3.7 was used to measure the effective spring constants of these melted joints on the soft robotic element with embedded PCL lattice. The desired axis was heated to 60 °C to melt the PCL polymer lattice along the axis, then the tendon was pulled with a load cell to measure the perpendicular force required to incur a 90 ° bend at the axis; average force measurements from 3 identical repeated tests were then converted to torsional spring constants listed in the table below. These values provide primitive estimates of the joint bending stiffnesses, but further testing is needed to confirm the constant stiffness assumption. The appropriate stiffness value ($k_{\text{straight}}, k_{\text{diagonal}}$, or k_{solid}) is selected in MATLAB based on the input axis selections.

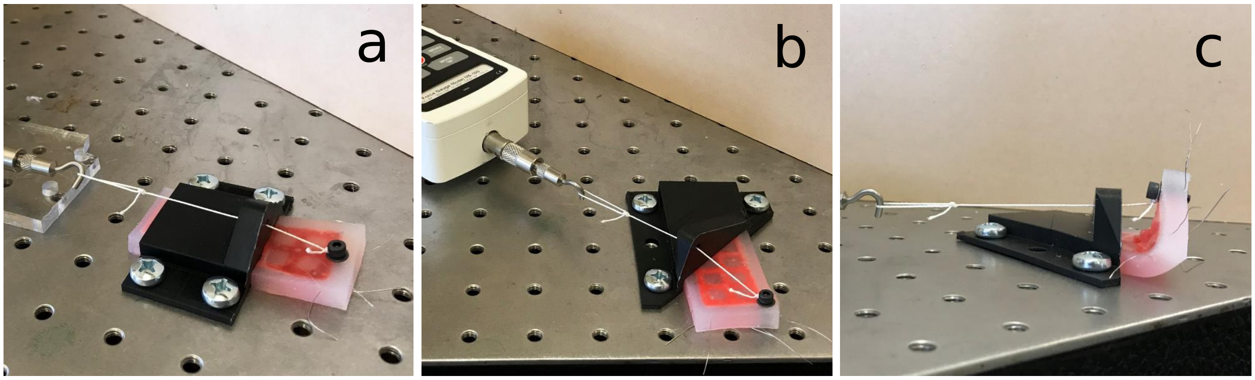

Figure 3.7 Setup for experimental testing of effective torsional spring constants for (a) transverse bending axis and (b)/(c) diagonal bending axis.

Table 3.1 Measured Torsional Spring Constants for Straight and Diagonal Axes

Axis Type	**Measured Spring Constant**	**Variable Name**
Straight (melted)	21.7 ± 1.4 N·mm/rad	$k_{straight}$
Diagonal (melted)	27.0 ± 1.0 N·mm/rad	$k_{diagonal}$
Straight (solid)	115 ± 11 N·mm/rad	k_{solid}

3.3.7 Relating Potential Energy to Joint Torques

The Euler-Lagrange method may be used to develop the equations of motion for the robotic element. Since we are only dealing with the statics of this problem, the higher order terms may be neglected. In other words, we can neglect the effects of kinetic energy and rotational inertia on the system. We will also choose to neglect gravity for this paper. By simplifying the problem in this way, the resulting governing equation will take the form:

$$\frac{-\partial \mathcal{L}(\theta, \omega)}{\partial \theta} = \tau^\top = K(\omega)\theta, \tag{3.15}$$

where $\mathcal{L}(\theta, \omega)$ is the Lagrangian, θ is the joint angles, and τ is the joint torques vector. Given that only potential energy is being considered in the system, the Lagrangian is simply equal to the negative of the potential energy from the joints. The torques generated by the bending at the joints are accounted for in the potential energy terms:

$$PE = -\mathcal{L} = \frac{1}{2}k_1\theta_1^2 + \frac{1}{2}k_2\theta_2^2 + \frac{1}{2}k_3\theta_3^2, \tag{3.16}$$

with k_i being the stiffness of the joint and θ_i being the angular displacement at that joint. Differentiating the Lagrangian with respect to θ yields

$$\frac{\partial \mathcal{L}}{\partial \theta} = \begin{bmatrix} -k_1\theta_1 & -k_2\theta_2 & -k_3\theta_3 \end{bmatrix}. \tag{3.17}$$

Applying the Euler-Lagrange equation to the simplified static model yields the following relationship

$$\tau^\top = -\frac{\partial \mathcal{L}}{\partial \theta} = \begin{bmatrix} k_1\theta_1 & k_2\theta_2 & k_3\theta_3 \end{bmatrix}. \tag{3.18}$$

By applying the relationship from Equation 3.11, the joint torques may be expressed in terms of the tendon forces and coupling matrix. Combining Equations 3.11 and 3.15 produces the relationship

$$K(\omega)\theta = P(\theta, \omega)f, \tag{3.19}$$

where $K(\omega)$ is the joint stiffness matrix:

$$K(\omega) = \begin{bmatrix} k_1(\omega) & 0 & 0 \\ 0 & k_2(\omega) & 0 \\ 0 & 0 & k_3(\omega) \end{bmatrix}. \tag{3.20}$$

In our system, we want to be able to determine θ given a particular f and ω. We also hope to determine f given θ and ω. To determine θ given f and ω, we left-multiply each side of Equation 3.19 by the inverse of the stiffness matrix to yield

$$\theta = K^{-1}(\omega)P(\theta,\omega)f. \tag{3.21}$$

The vector of joint angles θ cannot be solved analytically in this expression since the coupling matrix P is a complicated function of θ, and since θ appears on both sides of Equation 3.21. This equation can be solved numerically using fixed point iteration to determine the joint angles that result from a given set of selected axes ω and tendon forces f. To find the forces required to produce a desired set of joint angles, we simply left multiply Equation 3.19 by P-inverse to obtain:

$$f = P^{-1}(\theta,\omega)K(\omega)\theta. \tag{3.22}$$

3.4 Results and Discussion

3.4.1 Configuration Computation

A relationship has been developed that enables computation of the joint angles and configuration resulting from application of a given tendon force. For example, Figure 3.8 (a) shows the computed equilibrium configuration when a 4-Newton force is applied to the upper tendon, and the heating elements are activated to allow bending along axes $\omega_{1,1}$ and $\omega_{3,3}$. Other unique configurations may be achieved by applying different tendon forces and selectively melting different axes along the lattice, as seen in Figure 3.8 (b) and (c).

Various configurations may be used to perform intelligent tasks. For example, applying a 14-Newton force to the upper tendon while melting parallel diagonal axes could allow the robot to grab a pen as shown in Figure 3.9.

3.4.2 Workspace Limitations

It is interesting to note that Equation 3.21 fails to compute realistic joint angles if a joint angle exceeds 90° along a diagonal axis. At first glance, this may appear to be a computational

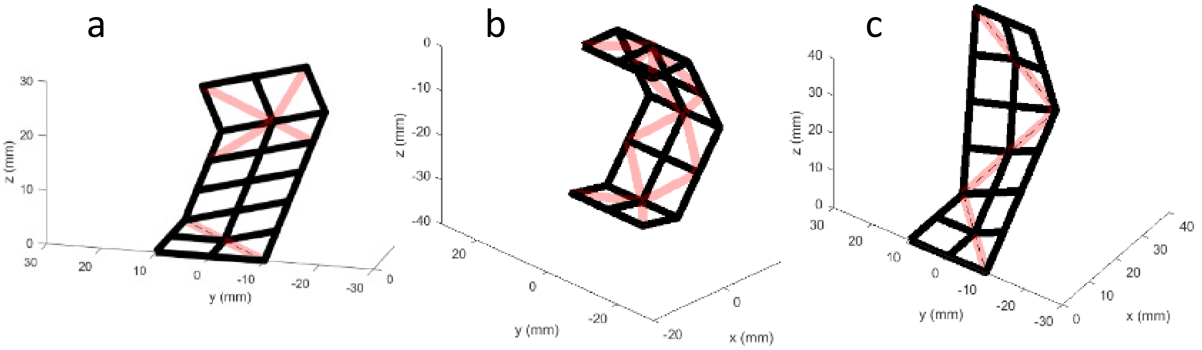

Figure 3.8 Simulated configurations of 3-link element under different heating and tendon loads, where red lines indicate activated heating elements.

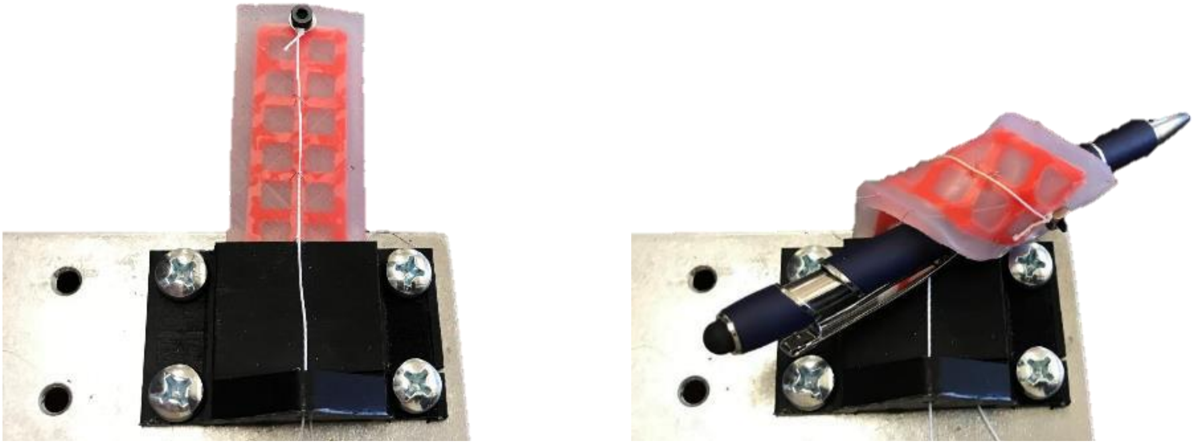

Figure 3.9 Melting parallel diagonal axes allows element to wrap around pen.

error, but in reality, this computational limitation perfectly represents a physical limitation. Careful inspection of the tendon routing shown in Figures 3.1 and 3.2 reveals the reason for this limitation. For this particular arrangement of tendon fixation points, the tendon length across a diagonal joint reaches a minimum when the joint angle is 90°. Bending a diagonal joint beyond 90° would actually require elongation of the tendon, so the physical model would never actually bend more than 90° along a diagonal axis. However, along the transverse axes, the physical element can bend beyond 90°, up to the point of folding on itself. This concept is again modeled perfectly by the mathematical model, which allows bending beyond 90° along transverse axes.

3.4.3 Force Computation

The ability to compute the tendon forces required to achieve a configuration is desirable for implementing advanced control with the soft robotic element. The relationship from Equation 3.22 enables this computation. For example, the configuration shown in Figure 3.8 (a) was achieved by applying a 4-Newton force to the upper tendon while melting axes $\omega_{1,1}$ and $\omega_{3,3}$. Applying Equation 3.21 revealed that this load/axis combination results in joint angles of 21.7°, 6.0°, and 93.9°, respectively. We can then test the validity of the force computation function by solving this problem backwards and comparing the force results with the original input force values. To do this, we use 21.7°, 6.0°, and 93.9° as the θ input in Equation 3.22, along with the axis selection $\omega_{1,1}$ and $\omega_{3,3}$ to determine the forces needed to achieve these joint angles. The forces computed should theoretically be 4 Newtons on the upper tendon and 0 Newtons on the lower tendon. Application of Equation 3.22 with these input values indicated that forces of 3.9992 N and -0.0009 N on the upper and lower tendons are required to achieve the particular configuration shown in Figure 3.8 (a). These results show that Equation 3.22 is useful for calculating the tendon forces required to achieve a desired set of joint angles with reasonable accuracy.

3.4.4 Joint Space Limitations

It is important to note that in the case of this 3-segment element with 2 opposing tendons, not all joint angle combinations are possible. The joint space is limited, and the required force computation only works when the desired joint angles lie within the allowable joint space. This detail is evidenced by both the physical model and the mathematics behind the force computation. From the physical model, we can intuitively see that the angles of the 3 simultaneously-melted joints cannot be controlled independently with the use of only one tendon. Here we consider only one tendon since it would be counter-productive to pull both tendons simultaneously. Increasing the tendon tension increases the joint angles of all three joints simultaneously in a specific ratio that is proportional to the relative bending stiffnesses of the three joints. In order to compute the tendon force required to achieve a desired set of joint angles, these joint angles must follow the proper ratio proportional to their bending stiffnesses. Otherwise, no tendon force will be able to cause joint angles that do not follow this ratio. For example, no tendon force will be able to cause bending in only the first joint if three joints are melted. Mathematically, this concept is demonstrated in the form of the coupling matrix P. Computing the required tendon forces involves multiplying by the inverse of P, as seen in Equation 3.22. Recall that P is a 3 × 2 matrix in this case. As such, the force computation only works when $\theta \epsilon Image[K^{-1}(\omega)P(\theta, \omega)]$. However, the restriction on θ for the force computation is actually even more stringent due to the tendon antagonism. Since one of the tendon forces is always zero, θ must be a scalar multiple of a single column of $[K^{-1}(\omega)P(\theta, \omega)]$ for computation of the tendon forces to be possible.

3.4.5 Grid Spacing

The grid spacing and width of the heating elements also affect the bending behavior of the lattice. As seen in Figure 3.4, each heating element melts a certain width of the lattice. When the width of the heated area is small relative to the grid size, more precise control can be achieved. On the other hand, when the width of the heated zone is large relative to the lattice grid size, the orientation of the axes may vary within the heated area. As shown in Figure 3.10, bending is allowed along any axis contained in the heated zone. This could result in imprecision in the motion of the lattice when the heating elements occupy a wide space. In the future, we hope to make lattices even smaller to enable more dexterous motions; this will require narrower heating elements to avoid diversion from the analytical model. Future work will quantify these effects by measuring deviations from the theoretical model caused by different grid spacings and element widths in the physical model.

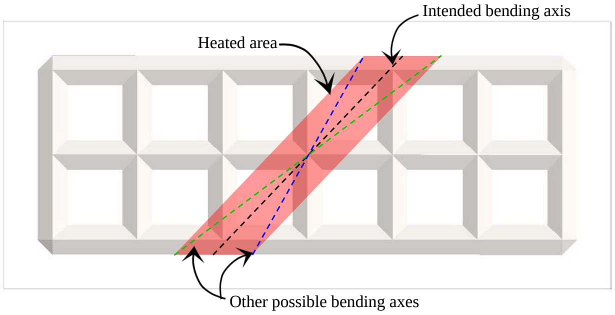

Figure 3.10 Effects of grid spacing and heating element width on bending axis precision. For this particular heated zone, bending is allowed along any axis between the green and blue axes. This could cause discrepancy between experimental and theoretical results if the analytical model is based on the intended bending axis but actual bending occurs about a different axis within the heated zone.

3.4.6 Effects of Successive Melting

By successively melting joints, a larger number of more complex configurations are made possible. Notably, it allows for the combination of movements which require both the top and bottom tendons to be pulled. As seen in Figure 3.11 (a) and (b), a single joint was melted to achieve a position by pulling the top and bottom tendons, respectively. With successive melting, these configurations can be combined to achieve the configuration shown in in Figure 3.11 (c). This combined configuration is not achievable with simultaneous melting, as both the top and bottom tendons must be pulled to achieve the final form. If both axes were melted simultaneously and each tendon pulled, the joints would not be able to bend in opposite directions like they can when sequentially melted.

3.5 Summary of Results

A relationship has been obtained to relate tendon forces to resulting joint angles and configuration in the static equilibrium of a 3-segment soft robotic element with selectable bending axes. With some limitations, this relationship can be used both ways: to compute joint angles given tendon forces and selected axes, or to compute necessary tendon forces to achieve desired joint angles for a given selection of axes. Using Equations 3.21 and 3.22, the joint

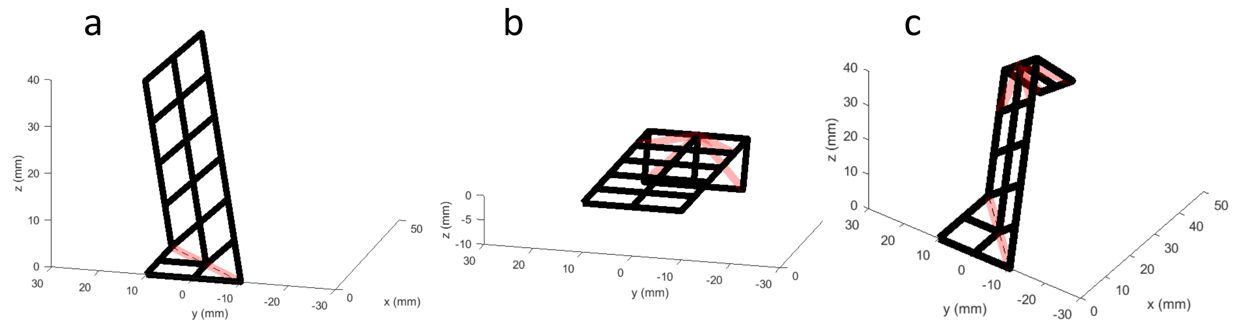

Figure 3.11 Example of 2-directional bending enabled by successive melting. (a) and (b) show individual steps; (c) shows resulting configuration from successive deformation.

angles are related to the required tendon forces using the coupling matrix. The joint stiffnesses were modeled as torsional springs with spring constants measured experimentally by melting a joint and pulling a perpendicular tendon using a force meter.

The next step for this project is to incorporate the dynamics of the system. For this static model, we have neglected the kinetic energy and rotational inertia components. Including these elements in the model will allow us to implement torque control in the future so that we may accurately control the movement of the element and achieve desired trajectories. In the future, it may be helpful to develop an intelligent method of determining which axes need to be melted in order to achieve a desired trajectory. This may be done by determining which set of axes make the desired trajectory lie within the image of the spatial manipulator jacobian. However, for this work the selected axes are a simple input.

Once these relationships are developed, they may then be applied to larger scale robotic elements that include more segments or even three-dimensional structures. We have seen in this project the unique configurations enabled by the selective melting of a small soft robotic element. With just one set of tendons and 3 joints, a wide variety of movements and configurations may be achieved, as evidenced by the ability to grasp a pencil, curl into a tight ball or extend out as a rigid arm. By applying these concepts into higher dimensional structures, highly dexterous movements even mimicking human gestures may be achieved.

Chapter Four

DUAL ANTAGONISTIC ACTUATION

Attribution:

This chapter is an original work, written by Emily Allen.

Contributions from:

John P. Swensen[1]

[1]School of Mechanical and Materials Engineering, Washington State University, Pullman, WA

4.1 Abstract

This paper presents the design of a new soft pneumatic actuator whose direction and magnitude of bending may be precisely controlled via activation of different shape memory alloy (SMA) springs within the actuator, in conjunction with pneumatic actuation. This design is inspired by examples seen in nature such as the human tongue, where the combination of hydrostatic pressure and contraction of intrinsic muscle groups enables precise maneuverability and morphing capabilities. Here, SMA springs are embedded in the walls of the actuator, serving as intrinsic muscles that may be selectively activated to constrain the device. The pneumatic SMA (PneuSMA) actuator demonstrates remarkable spatial controllability evidenced by testing under different pressures and SMA activation combinations. A finite element model is also developed to predict the actuator deformation under different pressure and activation conditions.

4.2 Introduction

Previously, the use of robots has been limited primarily to isolated environments for assembly, industrial fabrication, bomb diffusal, or other repetitive tasks. With the recent explosion of research in the field of soft robotics, this paradigm has shifted, enabling the use of soft robots for wearable medical devices, non-invasive biomedical equipment, helper robots, and other applications that require interaction with fragile objects or beings [99]. These applications demand the design of functional robots without heavy, rigid components that could harm the subject [24, 100].

Whereas traditional robot grippers and end effectors typically consist of rigid links with motors and cable systems to control motion about prismatic or revolute joints, soft robotics applications require the elimination of heavy, rigid parts that raise safety concerns. Thus, new strategies for actuation, structural integrity, and strength capabilities must be explored within the realm of soft materials [24, 90]. Maintaining the functionality and maneuverability of traditional robots while using soft materials is a challenging task as it complicates modeling/control schema and often requires the ability to control stiffness of the materials [2, 87]. Many researchers look to nature for inspiration in this field [12]. Biological examples such as the Venus Flytrap plant and muscular hydrostats such as the human tongue demonstrate remarkable stiffness control and morphing capabilities [54, 55]. In these natural examples, the combination of internal hydrostatic pressure and geometric constraints or localized muscle contraction enable deformation capabilities that many soft robotics researchers have attempted to reproduce [33, 91, 101].

Soft pneumatic actuators use compressed air as a driving force and are a popular approach to soft robotics as they contain no rigid parts. These actuators typically consist of a rubber chamber that is pressurized to cause expansion or motion in a direction determined by geometric or external constraints [68, 102]. Several different constraint strategies have been employed to cause different types of motions [91, 103].

One of the most well-known constraint types is seen in the McKibben Pneumatic Artificial Muscles (PAM's). These actuators are encased in a woven sleeve that transmits radial expansion into longitudinal contraction [104]. These PAM's offer a high strength-to-weight ratio with contractile behavior similar to human and animal muscles [67, 105–107].

In other pneumatic actuators, expansion is directed by means of geometric constraints imposed by the rubber itself [108, 109]. In these examples, the shape of the actuator causes more resistance to stretching in certain directions, resulting in nonuniform expansion. Often this is achieved with a thick wall on one side of the actuator that resists expansion more than the other walls, causing a bending motion [110].

Some pneumatic actuators utilize separate parallel channels or tubes within a single actuator [111–113]. These channels can then be selectively activated to cause bending in different directions. Dividing the channels into individually-controlled segments further improves controllability, although stiffness is still a concern.

Other researchers incorporate fibers as strain-limiting components, where different fiber arrangements cause different types of motions such as torsion, bending, and extension [114, 115]. Particularly relevant to this work is the PneuFLEX actuator by Deimel et al. [116], where fibers wrapped radially around the actuator constrain radial expansion, and additional fibers or inextensible fabric along one side of the actuator cause substantial bending upon inflation [92]. While these actuators offer desirable deformation capabilities, their motion is limited by the arrangement of the fibers within the actuator. Fiber-reinforced bending actuators are only capable of bending in one direction, predetermined by the placement of the fibers [114]. These actuators serve well as grippers, where only one direction of motion is required, but they lack more diverse posture variability [18, 116].

The pneumatic SMA (PneuSMA) actuator proposed in this is work is capable of multi-directional bending. Here shape memory alloy (SMA) coils are embedded along different sides of the actuator to act as "smart fibers." These coils are constraints that may be selectively activated by localized heating. The combination of radially-wrapped fibers and selective activation of the SMA coils enables bending with controllable magnitude and direction. This controllability drastically expands the workspace compared to simple pneumatic bending actuators. Variable stiffness can also be achieved by simultaneously pressurizing the chamber and activating SMA coils on opposite sides of the chamber.

Actuators similar to the proposed work include SMA-driven soft actuators by Taniguchi and Alcaide et al. [117, 118]. These actuators offer similar directional bending control via selective activation of different SMA coils. However, they incorporate air supply for the purpose of peristaltic motion or as a cooling mechanism rather than using the pneumatic pressure as a bending agonist with the SMA's as in the case of the PneuSMA actuator proposed here.

Others have employed similar dual actuation strategies, using tendons to control the bending direction of pneumatic actuators with activation of antagonistic groups enabling a high stiffness state [30, 31]. While these designs offer similar spatial controllability and stiffness control, they incorporate separate tendons for each independently-controlled segment of the actuator whereas the PneuSMA actuator includes only one SMA spring along each bending direction. Different segments of a single SMA coil may be activated in the PneuSMA actuator to control bending in any segment of the actuator.

4.3 Materials and Methods

4.3.1 Actuator Design

The design of the PneuSMA Actuator shown in Figure 4.1 is inspired by the PneuNet and PneuFLEX continuous actuators which are capable of bending tightly upon pressurization. While the PneuNet and PneuFLEX actuators utilize solely fibers as geometric constraints, the PneuSMA actuator incorporates both fibers and SMA coils which serve as constraints that may be selectively activated to offer precise spatial control.

The design of this actuator exploits the principle of anisotropic elasticity. Fibers wrapped helically along the length of the actuator prevent radial expansion, thus forcing longitudinal elongation. The SMA coils along the sides hinder elongation of one side of the actuator when activated by a heat stimulus. Due to the shape memory effect, the pre-stretched SMA coils exert a shortening force along one side of the actuator when heated via electrical current.

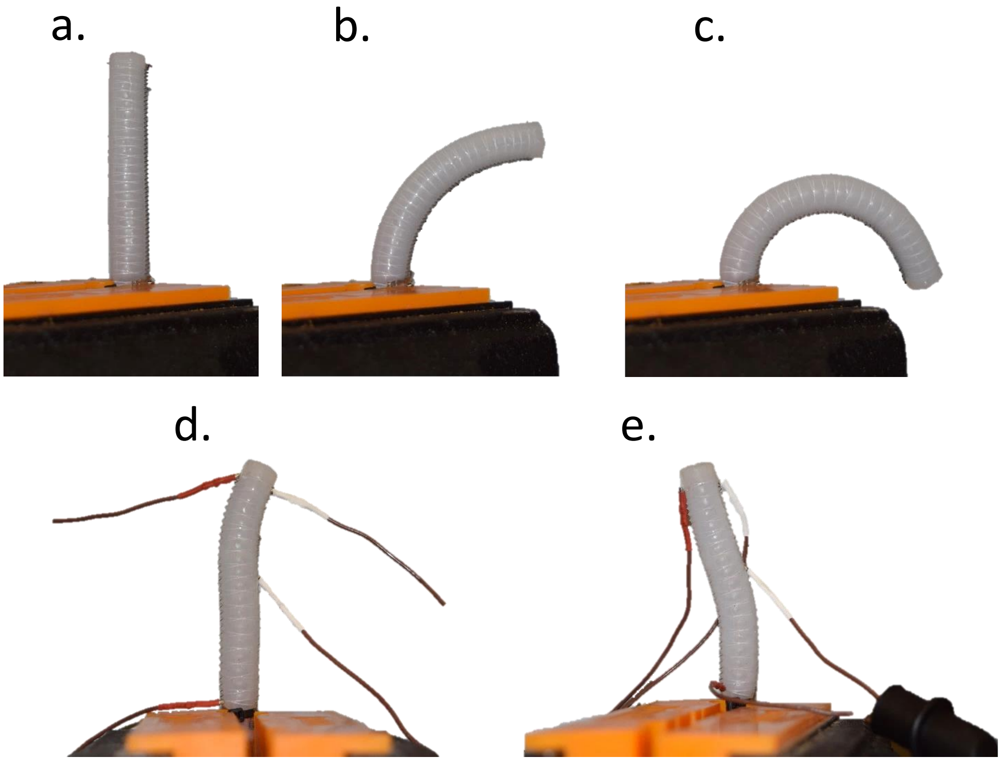

Figure 4.1 Controlled deformation capabilities of PneuSMA actuator. (a)-(c) show the bending of a PneuSMA actuator with 2 side-by-side SMA coils embedded along the right side, with increasing internal pressure from left to right. (d) and (e) show selective activation of coil segments along both the left and right sides of the actuator.

Meanwhile, the rest of the actuator extends longitudinally due to the internal pressure and radial constraint. The combination of the internal pressure and the SMA spring force results in substantial bending of the actuator. As shown in Figure 4.1, the actuator may be precisely controlled by heating different segments of the coils.

4.3.2 Actuator Fabrication

Fabrication of the actuator requires minimal supplies and equipment. Dragon Skin^{TM} 20 Silicone was used for the main body of the actuator. The other assembly materials, include polyester sewing thread, 4mm x 6mm PVC tubing, 0.25mm x 0.9mm Nitinol micro spring (tight pitch), 3D printed ABS mold and core, Sil-Poxy silicone glue, and a small cable tie.

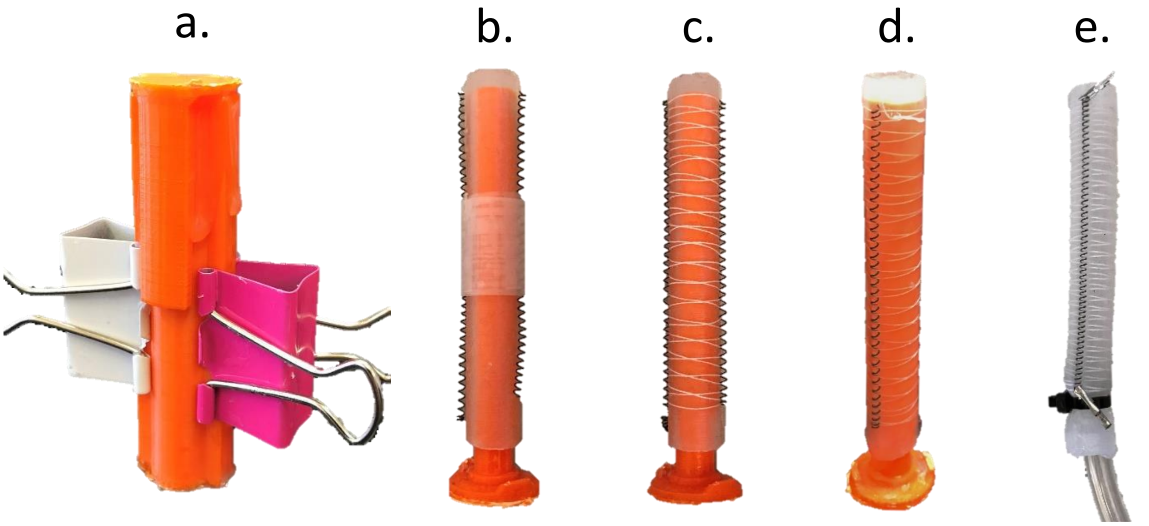

Figure 4.2 PneuSMA Actuator fabrication steps including (a) casting of silicone tube, (b) placement of pre-stretched Nitinol coils, (c) wrapping of the radial fibers around SMA springs, (d) thin coating of silicone over fibers, and (e) completed actuator.

To assemble the actuator, the plastic mold pieces are sprayed with Mold-Release spray to prevent adhesion of the silicone to the mold. The liquid silicone parts A and B are mixed together in equal parts by mass then degassed in a vaccuum chamber. As shown in Figure 4.2 (a), the outer mold pieces are then clamped together and filled with the prepared liquid silicone before the plastic core is inserted. The outer mold pieces are removed once the silicone has cured for at least 4 hours. Next, the Nitinol coils are pre-stretched to 4 times their original length. This 300% spring strain corresponds to about 6% strain of the Nitinol material. The coils are then positioned along the sides of the silicone and temporarily secured with tape as seen in Figure 4.2 (b).

As shown in Figure 4.2 (c), the thread fiber is wrapped in a double helix pattern around the actuator with one thread passing between each coil of the Nitinol. The thread is wrapped spirally starting from the tip, skipping every other coil. Then once wrapped all the way to the base, the wrapping continues spirally outward, back to the tip, passing through each of the skipped coils. The two ends of the threads are then tied together and trimmed. To secure the fibers in place, a second layer of liquid silicone is spread thinly over the fibers as seen in Figure 4.2 (d). Once cured, the plastic core is removed, and the PVC tubing is inserted in the opening. A small amount of silicone glue and a cable tie seal the opening around the supply tube. Figure 4.2 (e) shows the completed actuator.

4.3.3 Test Setup and Procedure

In this work, testing of the actuators is designed for the following objectives:

- Demonstrate the spatial controllability that may be achieved by selectively activating different coil segments.
- Assess the effectiveness of multiple SMA coils in increasing actuator curvature.
- Compare the bending behavior of the SMA-driven PneuSMA actuator with the behavior of a purely fiber-reinforced actuator.
- Compare FEA model with experimentally-measured actuator curvatures.

To assess these objectives, five different actuators were constructed as shown in Figure 4.3. Actuators (a) and (b) respectively have 1 and 2 side-by-side coils along one side of the actuator. Actuator (c) has no SMA coils but instead has a Nylon fiber embedded along one side of the actuator to serve as an inextensible constraint. Actuator (d) has one coil along each side of the actuator with conductive wires attached at different locations along the coils for selective heating. Actuators (a) - (d) have an outer diameter of 10 mm. Actuator (e) has one SMA spring along one side and has a smaller overall diameter than the others (6mm).

The test setup is shown in Figure 4.3 (f) where the actuator is clamped in a vice with the supply tube attached to a large syringe. A force gauge attached to a Mark10 test stand is then lowered to compress the plunger in the syringe and pressurize the actuator.

During testing, the force cell is lowered continuously on the syringe, gradually pressurizing the actuator. Side-view photos are captured to record the deformed shape of the actuator as the pressure increases. These photos are analyzed afterwards to determine the bend radius

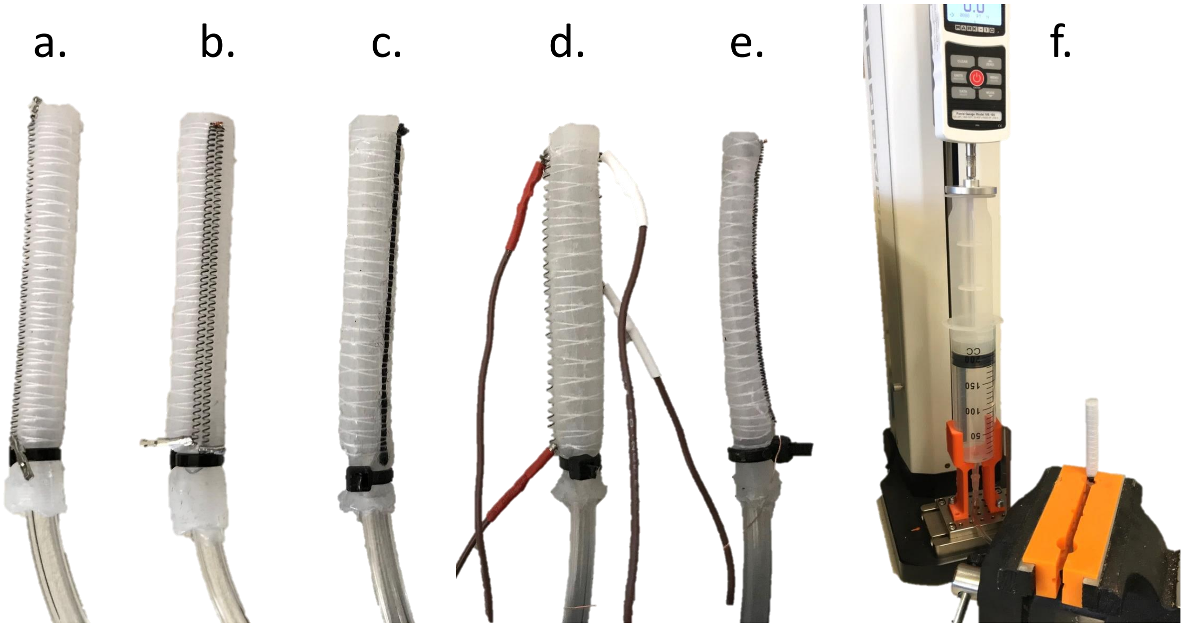

Figure 4.3 Fabricated samples and bend test setup. Actuators (a) and (b) contain 1 and 2 side-by-side coils along one side; actuator (c) contains a nylon fiber along one side; actuator (d) contains one coil along each side; and actuator (e) contains a single coil on one side and has a smaller overall diameter.

of the actuator, and the corresponding force on the syringe is used to calculate the internal pressure based on the area of the plunger.

4.3.4 Finite Element Modeling

The bending of the PneuSMA actuator is described using a simplified modeling approached based on the stiffness of the silicone rubber and finite element analysis of parallel springs along the length of the actuator as shown in Figs. 4.4 and 4.5.

In modeling the bending of a PneuSMA actuator with SMA coils along one side only, we begin by accounting for the lengthening of the actuator due to the pressure on the inside walls of the actuator. This elongation and the related dimmensions are shown in Figure 4.4. The outside walls of the actuator are assumed to be fixed at a constant diameter since the close-packed helical fibers prevent significant radial expansion. The silicone rubber has a Poisson's ratio of 0.47 - 0.49 reported in the literature, indicating that the material is

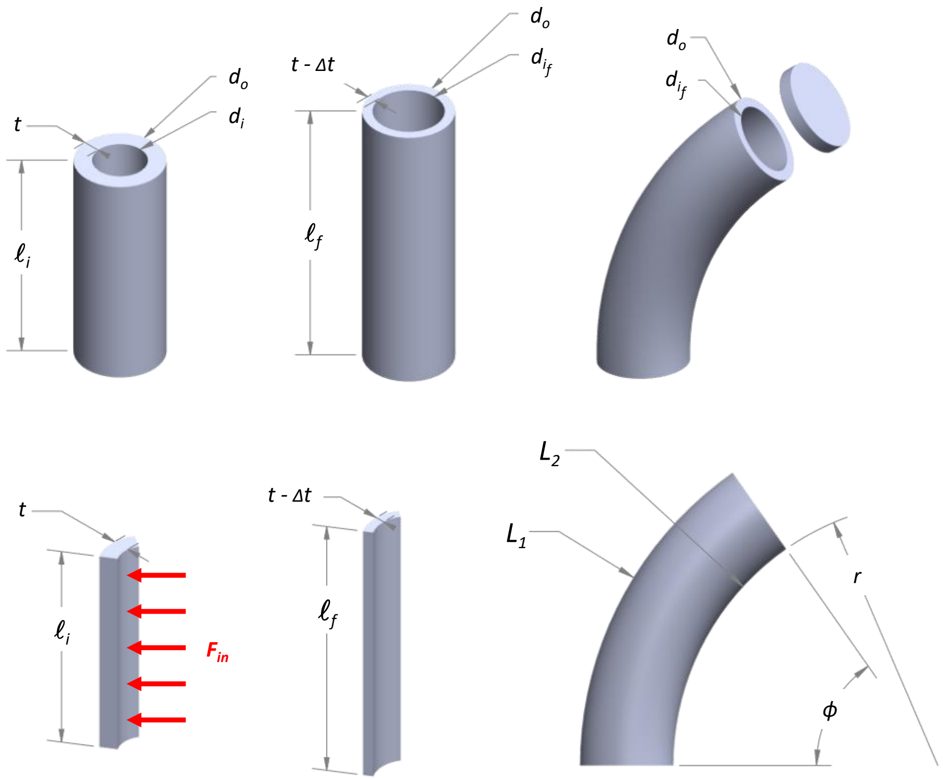

Figure 4.4 PneuSMA actuator dimensions and modeling steps.

nearly incompressible. Thus, it is reasonable to assume that any compression of the inner walls results in elongation of the actuator if we impose a constant volume constraint on the silicone material. The change in thickness of the actuator walls Δt can be expressed using the stiffness of the silicone material to describe the compression:

$$F_{in} = PA_{in} = \frac{EA_{in}}{t}\Delta t \qquad \Rightarrow \qquad \Delta t = \frac{Pt}{E}\,, \tag{4.1}$$

where A_{in} is the surface area of the inner walls of the actuator, E is the elastic modulus of the silicone, and P is the internal pressure. The silicone material has a nonlinear elastic response, so the secant modulus obtained from tension and compression testing is used to characterize the silicone stiffness. The tension and compression test data is shown in Figure A.1.

The resulting length of the actuator can then be calculated as a function of pressure by

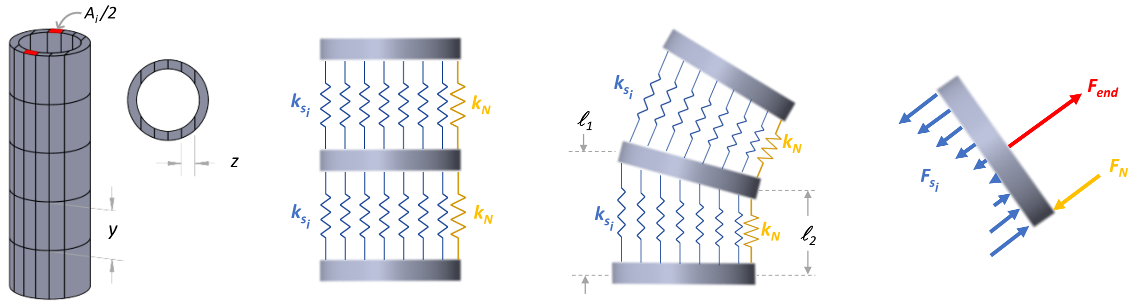

Figure 4.5 Schematic discretization of PneuSMA actuator for finite element analysis where forces acting on the end of the actuator are shown on the right.

imposing the silicone constant volume constraint:

$$\ell_f = \frac{A_{initial}}{A_{final}}\ell_i = \frac{d_o^2 - d_i^2}{d_o^2 - (d_o - 2[t - \frac{Pt}{E}])^2}\,\ell_i, \tag{4.2}$$

where $A_{initial}$ and A_{final} refer to the annular cross-sectional area of the actuator before and after pressurization.

Now to account for the actuator bending, we discretize the actuator to model the bending stiffness of the silicone and the compressive force of the Nitinol as a system of springs as shown in Figure 4.5. The actuator is divided into 1,000 segments along both its length and width, resulting in 1,000,000 total springs representing the silicone, in addition to 1,000 springs in series along the right side to model the Nitinol spring force. A zero displacement boundary condition exists at the base of the actuator where it is clamped in the vice, and an external force acts on the last segment of the actuator due to the internal pressure acting on the end of the actuator. This end force is simply

$$F_{end} = P\frac{\pi}{4}d_{i_f}^2 = P\frac{\pi}{4}(d_o - 2[t - \Delta t])^2, \tag{4.3}$$

where d_{i_f} is the inner diameter of the tube after lengthening from internal pressure. The stiffness of each silicone spring element depends on the silicone modulus E, the length of the spring y, and the effective area of each spring A_i:

$$k_{s_i} = \frac{EA_i}{y}. \tag{4.4}$$

Again, the silicone secant modulus is used to describe the nonlinear stiffness.

As seen in Figure 4.5, the lengths of all spring elements are identical, but the effective area varies along the width of the actuator due to the annular cross section. Thus, all springs in series have the same stiffness, but parallel springs have different stiffness values. The rest length of each of the silicone springs is simply

$$y = \frac{\ell_f}{m} = \frac{\ell_f}{1000}, \tag{4.5}$$

where m is the number of spring segments in series.

The Nitinol spring stiffness was measured experimentally with 10 mm rest length springs in the Austenite phase. Data from the Nitinol spring tension tests is shown in Figure A.2. The stiffness of the Nitinol springs is not perfectly linear, so the secant stiffness is used to account for this nonlinearity in the model. The nonlinear stiffness of each Nitinol spring element in the model is then scaled for the length of the discrete elements. A 15 mm rest length spring was used for these actuators, so the spring constant of each element is then scaled by this spring length and the number of series elements m:

$$k_N = m\left(\frac{10\,\mathrm{mm}}{15\,\mathrm{mm}}\right)k_{N_{measured}}\,. \tag{4.6}$$

It is important to note that the rest length of the Nitinol spring elements is not the same as the rest length of the silicone spring elements. Becuase the Nitinol coils were prestretched before being attached to the actuator, they have a much shorter rest length:

$$\ell_{0_N} = \frac{15\,\mathrm{mm}}{m} = \frac{15\,\mathrm{mm}}{1000} = 0.015\,\mathrm{mm}. \tag{4.7}$$

Assuming that each set of parallel springs stretches or compresses to some new length ℓ_1 on the left side of the actuator and ℓ_2 on the right side, the tensile force in each Nitinol spring element can be expressed as

$$F_N = k_N(\ell_2 - \ell_{0_N}). \tag{4.8}$$

The tensile force in each silicone spring element can then be expressed as

$$F_{s_i} = k_{s_i}(\ell_i - y), \tag{4.9}$$

where ℓ_i is the length of the i^{th} spring element, determined by linear interpolation between ℓ_1 and ℓ_2 shown in Figure 4.5. Here a negative force indicates compression.

The resulting shape of the actuator is determined by varying the element stretch lengths ℓ_1 and ℓ_2 until a static force and moment balance is achieved, including the external force F_{end}. MATLAB's built-in fminsearch function was used to determine the element stretch lengths that minimize residuals in the force and moment balance.

The radius of curvature r from Figure 4.4 is defined using the sum of the element side lengths:

$$\kappa = \frac{1}{r} = \frac{L_1/L_2 - 1}{d_o} = \frac{\sum \ell_1 / \sum \ell_2 - 1}{d_o}. \tag{4.10}$$

4.4 Results and Discussion

4.4.1 Precise Spatial Maneuverability

The PneuSMA actuator demonstrated overall precise spatial maneuverability enabled by the selective actuation of different coil segments. Figure 4.1 (a) through (c) show the bending of actuator (b) which contains two side-by-side SMA coils along the right side. Here the bend radius is controlled by the pressure applied to the actuator supply, and an increase in pressure causes tighter bending as seen in Figure 4.1 (c).

Figure 4.1 (d) and (e) show the deformation of actuator (d) which contains one SMA coil along each side. In Figure 4.1 (d), the top section only of the right coil is heated while the left coil and the bottom of the right coil remain at room temperature. This causes localized bending to the right precisely at the tip of the actuator. In Figure 4.1 (e), the entire length of the left side coils are heated as well as the upper half of the right side coils. The bottom half of the right side coils remain at room temperature, allowing bending to the left precisely at the base of the actuator.

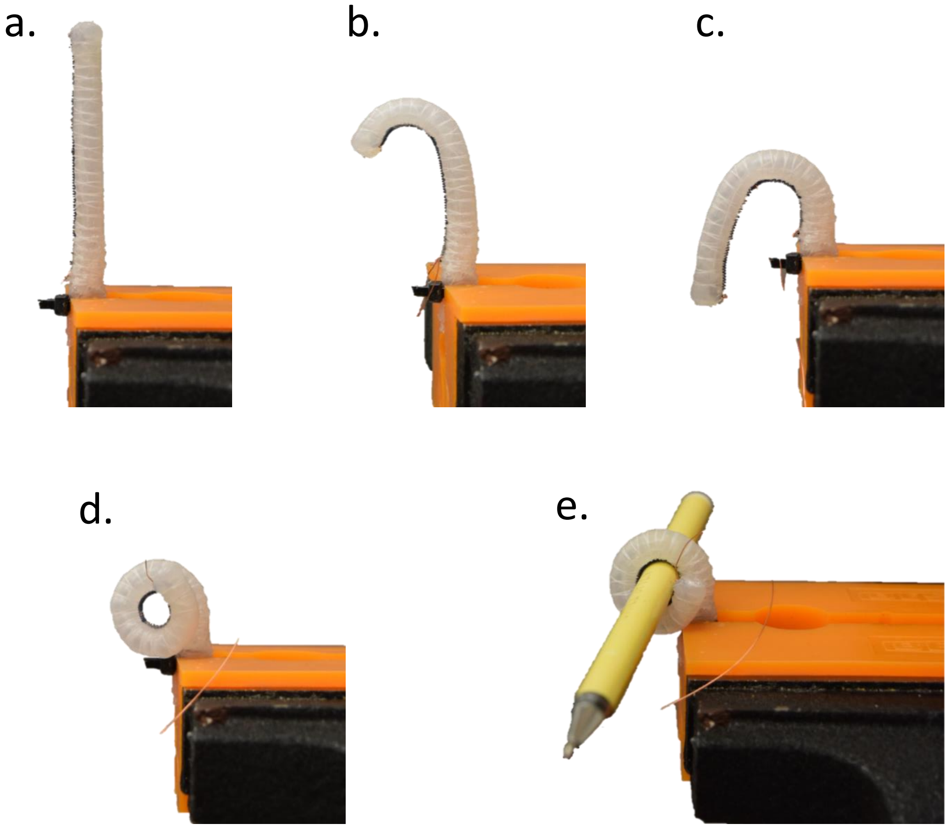

Figure 4.6 Demonstrated spatial maneuverability and tight curvature with narrow PneuSMA actuator.

Figure 4.6 shows the maneuverability of the narrow actuator (e) which can achieve a tight bend radius, even wrapping around an 8mm pen. Its narrow body enables tight curvature and proves that these actuators can be scaled down for use in space-constrained medical applications. In Figure 4.6 (b) and (c), different segments of the SMA spring is activated to cause individual control of distal and proximal bending, respectively.

4.4.2 Tighter Bending with Multiple Side-By-Side Coils

Actuators (a), (b), and (c) were tested at a variety of pressures while the coils were fully activated to assess the effectiveness of additional coils to increase the curvature at any given pressure. The data points in Figure 4.7 show the curvature measured for each of the three actuators at different pressures. The bend data shows higher curvature in the PneuSMA actuators with more coils for any given pressure. Thus, additional coils enable tighter bending of the actuator, as expected.

The green data points in Figure 4.7 show the measured curvature of the fibers-only actuator, actuator (c). Overall, the PneuSMA actuators exhibit significantly higher curvatures than the PneuFLEX actuator (c). At low pressures, the SMA-driven actuator (a) outperforms the fiber-only actuator, but at pressures above about 140 kPa, the opposite is true. This makes sense since the SMA coils are not inextensible; they can offer some compression at low pressures but also suffer some elongation at high pressures.

4.4.3 Modeling Results

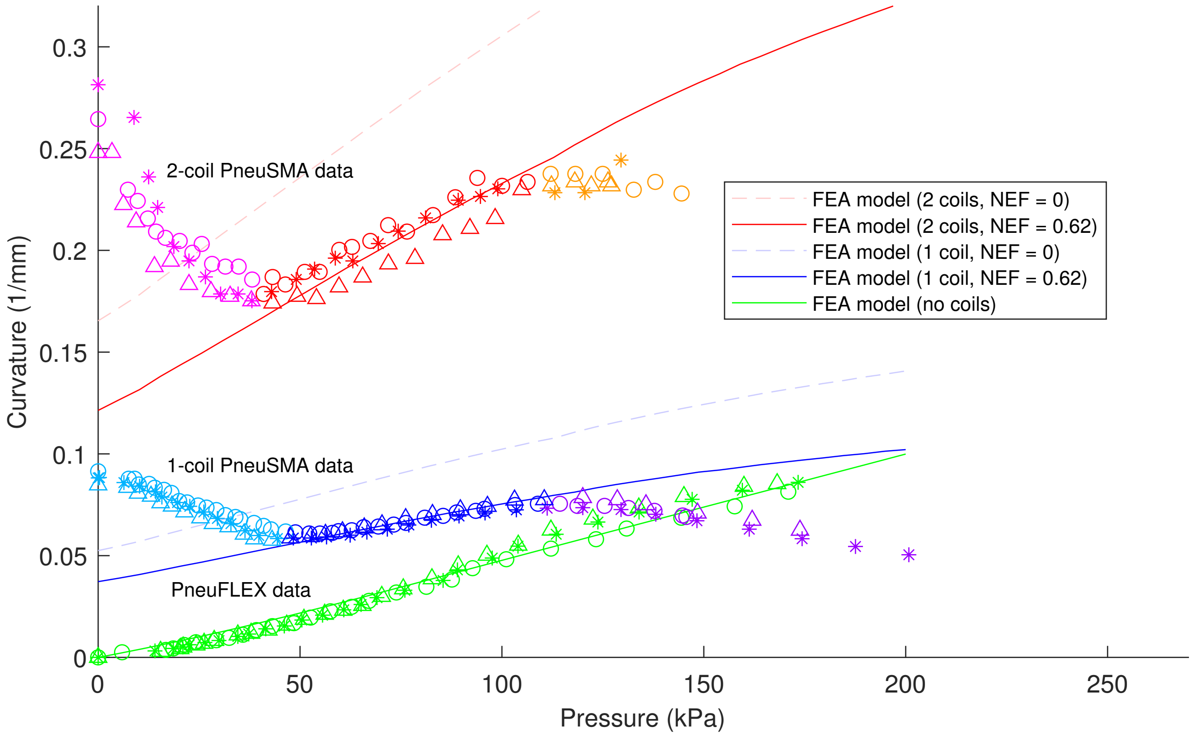

Figure 4.7 Comparison of FEA model with measured bending behavior.

The curvatures predicted by the finite element model are shown by the solid curves in Figure 4.7. From this plot, it can be seen that the model accurately describes the curvature of the fiber-only (PneuXLEX) actuator across the entire range of pressures tested. The model-predicted curvatures for the SMA-driven actuators also match the experimental measurements within the appropriate pressure range. At low pressures (below about 45 kPa), the PneuSMA actuators buckle when the SMA coils are activated because the low internal pressure is insufficient to prevent the actuator from collapsing on itself under the compressive force from the coils. The FEA model does not account for buckling, so this unstable behavior is not matched by the model. This buckling behavior explains the deviation between the model and data at low pressures in Figure 4.7. At high pressures (above about 110 kPa), the measured curvatures again deviate from the model prediction as the actuator begins to straighten and resist the contraction of the SMA coils. This straightening at high pressures can likely be attributed to the Bourdon effect, the principle at work in Bourdon pressure gauges where the force imbalance between the inner and outer sides of the curved tube cause straightening as internal pressure is increased. This effect produces undesirable straightening of the PneuSMA actuators at high pressures which should be avoided in practical applications. Thus, the PneuSMA actuators should be designed for use at moderate pressures, above the buckling region but below the Bourdon straightening region.

The Nitinol effectiveness factor (NEF) accounts for the restraints on the Nitinol coils that prevent compression of the springs and reduce the overall shortening force exerted by the springs. The thin polyester threads hold each coil of the springs rigidly in place along the silicone actuator. This silicone material contributes resistance to the spring shortening that must be accounted for with the NEF. An NEF value of 0.62 was found to fit the experimental data. This factor proves consistent for both the 1-coil and 2-coil PneuSMA actuators as shown in Figure 4.7.

4.5 Summary of Results

We presented the novel design of a pneumatic soft actuator with embedded SMA coils that serve as intrinsic muscle fibers to direct the deformation. Different segments along the actuator may be independently controlled via heating of selective SMA spring segments without requiring separate tendons for each segment or lengthy tendon routes. The actuator demonstrated highly dexterous capabilities that make it well-suited for soft end effectors that operate in delicate environments requiring precise maneuverability. The actuators can be made as thin as 6mm with a radius of curvature down to less than 4mm. A finite element model has been developed that predicts the bend curvature based on internal pressure and SMA activation. The actuator is entirely biocompatible and may lend itself well to biomedical devices such as catheters or colonoscopes. The next steps in adapting the design for these types of applications will include making the actuator thinner than the current 10 mm and 6 mm designs and embedding the SMA springs internally where the heat activation would be shielded from surrounding tissue. A pneumatic venting system could then dissipate heat from the internal SMA coils. The actuator may be further improved by including more intrinsic muscles to enable even finer control of stiffness and bending.

Chapter Five

CONCLUSION

Attribution:

This chapter is original work written by Emily Allen.

5.1 Summary

The objective of this research was to investigate and design materials, geometric patterns, and antagonistic actuation arrangements that result in structures whose magnitude and direction of stiffness may be controlled independently of their motion. A brief introduction to soft robotics and variable stiffness structures was provided in chapter 1 to demonstrate the context and motivation of this research. The remaining chapters discussed the design and evaluation of variable stiffness smart composite materials, geometrically-patterned variable stiffness structures, and dual antagonistic actuation devices, respectively. Key conclusions from these works are summarized below.

5.1.1 Smart Material Composites

- Combining multiple smart materials in a single composite resulted in additional stiffness levels activated by a temperature stimulus. The PCL/Nitinol composite, for example, demonstrated a high-low-medium stiffness sequence when heated from room temperature.
- A visible correlation was identified between the stiffness of the smart material composites and that of the constituent materials.
- The transition temperatures of individual smart materials may be tuned by varying the alloy compositions. For composites with multiple stiffness levels, smart materials

with noticeably different transition temperatures should be incorporated to maximize the number of discrete stiffness levels.

- The inclusion of more smart materials enables more stiffness levels, resulting in finer control of soft robotic structures.

5.1.2 Geometric Design and Control

- A soft robotic structure with directional stiffness control capabilities was fabricated by encasing a low melting point material lattice structure in silicone rubber with localized heating elements to control the axes of compliance.
- The product of exponentials formulation was successfully applied to the variable stiffness lattice piece to develop the forward kinematics relationships.
- A relationship was obtained to relate tendon forces and joint angles for any selection of axes by modeling melted joints as torsional springs.
- The physical structure demonstrated unique spacial maneuverability matching the configurations predicted by the kinetic model.
- Limitations in the work space of the physical element are also evidenced mathematically in the kinetic model developed.
- Successively melting, deforming, and re-solidifying the element enables independent control of joint angles with a single tendon. The effective work space of the element is thus dramatically expanded by activating the compliance axes sequentially.

5.1.3 Dual Antagonistic Actuation

- Shape memory alloy coils embedded in parallel with a pneumatic actuator enabled independent control of stiffness and deformation.

- The proposed PneuSMA actuator demonstrated higher curvature and control of more degrees of freedom than the PneuFLEX actuator which uses inextensible fibers in place of the SMA coils used in this work.
- The PneuSMA actuator was made as small as 6 mm in diameter and has no rigid components, making it ideal for minimally invasive medical devices such as catheters and colonoscopes.
- A finite element model was developed that successfully predicts the bend curvature of the PneuSMA actuator within a practical pressure range. The practical pressure range is limited by undesirable buckling at low pressures and straightening due to the Bourdon effect at high pressures.

5.2 Applications and Future Work

Variable stiffness structures lend themselves to a wide variety of soft robotics applications ranging from medical equipment to personal robots and wearable devices.

The inclusion of multiple smart materials in a single composite could enable soft robots with finely tunable stiffness, capable of 'compliance matching' for a broad variety of tasks. Helper robots made with smart material composites could exert the force needed to lift a person out of bed one moment, then gingerly offer a compliant hug the next moment. Future research will need to address the challenge of heat dissipation—possibly via flexible heat pipes, conductive particulate additives, or coolant circulation—in order to improve cycling time.

Soft robot structures with directional stiffness control may be especially useful for tasks that simultaneously require high strength in one direction and compliance in another. For example, the task of squeezing through a tight space or wrapping around complicated shapes while maintaining the strength to lift the object without deforming its shape would require control of compliance axes. The low melting point skeleton structures are particularly useful in these situations as they can morph freely around a uniquely-shaped object, then re-solidify in this new shape before exerting force to move or bend the object. Again, the issue of heat dissipation needs to be addressed, and further study of expanded geometries is needed to develop 3D morphable structures with directional stiffness control.

The pneumatic SMA actuator shows promise for application in medical devices due to its compact size and biocompatible, soft materials. The independent control of bending and stiffness is essential for endoscopic and arthroscopic tools where the device needs to deform easily through delicate channels then exert forces needed to cut tissue, collect samples, etc. Furthermore, the shape memory alloy actuation eliminates the need for numerous tendons and routing schema. Next, a new fabrication method is needed for embedding the SMA coils on the inside of the actuator tube so that delicate bodily tissues would be protected from the heated coils.

REFERENCES

[1] Fumiya Iida and Cecilia Laschi. “Soft Robotics: Challenges and Perspectives”. In: *Proceedings Of The 2Nd European Future Technologies Conference And Exhibition 2011 (Fet 11)*. Procedia Computer Science 7 (2011), pp. 99–102. DOI: 10.1016/j.procs.2011.12.030. URL: http://infoscience.epfl.ch/record/178736.

[2] Sangbae Kim, Cecilia Laschi, and Barry Trimmer. “Soft robotics: a bioinspired evolution in robotics”. In: *Trends in Biotechnology* 31.5 (2013), pp. 287–294. ISSN: 0167-7799. DOI: https://doi.org/10.1016/j.tibtech.2013.03.002. URL: http://www.sciencedirect.com/science/article/pii/S0167779913000632.

[3] Cecilia Laschi, Barbara Mazzolai, and Matteo Cianchetti. “Soft robotics: Technologies and systems pushing the boundaries of robot abilities”. In: *Science Robotics* 1.1 (2016). DOI: 10.1126/scirobotics.aah3690. eprint: https://robotics.sciencemag.org/content/1/1/eaah3690.full.pdf. URL: https://robotics.sciencemag.org/content/1/1/eaah3690.

[4] Loïc Blanc, Alain Delchambre, and Pierre Lambert. “Flexible Medical Devices: Review of Controllable Stiffness Solutions”. In: *Actuators* 6.3 (2017). ISSN: 2076-0825. DOI: 10.3390/act6030023. URL: https://www.mdpi.com/2076-0825/6/3/23.

[5] Alexander G. Volkov et al. “Kinetics and Mechanism of Dionaea muscipula Trap Closing”. In: *Plant Physiology* 146.2 (2008), pp. 694–702. ISSN: 0032-0889. DOI: 10.1104/pp.107.108241. eprint: http://www.plantphysiol.org/content/146/2/694.full.pdf. URL: http://www.plantphysiol.org/content/146/2/694.

[6] Winfried Peters, Wolfgang Hagemann, and Alun Tomos. “What makes plants different? Principles of extracellular matrix function in ’soft’ plant tissues”. In: *Comparative biochemistry and physiology. Part A, Molecular integrative physiology* 125 (Mar. 2000), pp. 151–67. DOI: 10.1016/S1095-6433(99)00177-4.

[7] Vitaly Napadow et al. “Intramural mechanics of the human tongue in association with physiological deformations.” In: *Journal of biomechanics* 32 1 (1999), pp. 1–12.

[8] Matteo Cianchetti et al. “Bioinspired locomotion and grasping in water: The soft eight-arm OCTOPUS robot”. In: *Bioinspiration amp Biomimetics* 10 (Mar. 2015). DOI: 10.1088/1748-3190/10/3/035003.

[9] Kathryn A Daltorio et al. “Efficient worm-like locomotion: slip and control of soft-bodied peristaltic robots”. In: *Bioinspiration & Biomimetics* 8.3 (Aug. 2013), p. 035003. DOI: 10.1088/1748-3182/8/3/035003. URL: https://doi.org/10.1088%2F1748-3182%2F8%2F3%2F035003.

[10] J. Koh and K. Cho. “Omegabot : Biomimetic inchworm robot using SMA coil actuator and smart composite microstructures (SCM)”. In: *2009 IEEE International*

Conference on Robotics and Biomimetics (ROBIO). Dec. 2009, pp. 1154–1159. DOI: 10.1109/ROBIO.2009.5420752.

[11] Joey Z Ge et al. “An earthworm-inspired friction-controlled soft robot capable of bidirectional locomotion”. In: *Bioinspiration & Biomimetics* 14.3 (Feb. 2019), p. 036004. DOI: 10.1088/1748-3190/aae7bb. URL: https://doi.org/10.1088%2F1748-3190%2Faae7bb.

[12] Deepak Trivedi et al. “Soft Robotics: Biological Inspiration, State of the Art, and Future Research”. In: *Applied Bionics and Biomechanics* 5 (Oct. 2008), pp. 99–117. DOI: 10.1080/11762320802557865.

[13] Chiwon Lee et al. “Soft robot review”. In: *International Journal of Control, Automation and Systems* 15 (Jan. 2017). DOI: 10.1007/s12555-016-0462-3.

[14] Pinar Boyraz, Gundula Runge, and Annika Raatz. “An Overview of Novel Actuators for Soft Robotics”. In: *Actuators* 7 (Aug. 2018), p. 48. DOI: 10.3390/act7030048.

[15] Iain A. Anderson et al. “Multi-functional dielectric elastomer artificial muscles for soft and smart machines”. In: *Journal of Applied Physics* 112.4 (2012), p. 041101. DOI: 10.1063/1.4740023. eprint: https://doi.org/10.1063/1.4740023. URL: https://doi.org/10.1063/1.4740023.

[16] Matteo Cianchetti et al. “A new design methodology of electrostrictive actuators for bio-inspired robotics”. In: *Sensors and Actuators B: Chemical* 142 (Oct. 2009), pp. 288–297. DOI: 10.1016/j.snb.2009.08.039.

[17] S. Kim et al. “Micro artificial muscle fiber using NiTi spring for soft robotics”. In: *2009 IEEE/RSJ International Conference on Intelligent Robots and Systems*. Oct. 2009, pp. 2228–2234. DOI: 10.1109/IROS.2009.5354178.

[18] Raphael Deimel and Oliver Brock. “A novel type of compliant and underactuated robotic hand for dexterous grasping”. In: *The International Journal of Robotics Research* 35.1-3 (2016), pp. 161–185. DOI: 10.1177/0278364915592961. eprint: https://doi.org/10.1177/0278364915592961. URL: https://doi.org/10.1177/0278364915592961.

[19] James Walker et al. “Soft Robotics: A Review of Recent Developments of Pneumatic Soft Actuators”. In: *Actuators* 9.1 (2020). ISSN: 2076-0825. DOI: 10.3390/act9010003. URL: https://www.mdpi.com/2076-0825/9/1/3.

[20] M. Wehner et al. “Experimental characterization of components for active soft orthotics”. In: *2012 4th IEEE RAS EMBS International Conference on Biomedical Robotics and Biomechatronics (BioRob)*. June 2012, pp. 1586–1592. DOI: 10.1109/BioRob.2012.6290903.

[21] Robert F. Shepherd et al. “Multigait soft robot”. In: *Proceedings of the National Academy of Sciences* 108.51 (2011), pp. 20400–20403. ISSN: 0027-8424. DOI: 10.1073/

pnas.1116564108. eprint: https://www.pnas.org/content/108/51/20400.full.pdf. URL: https://www.pnas.org/content/108/51/20400.

[22] Elango Natarajan and Ahmad Athif Mohd Faudzi. "A review article: Investigations on soft materials for soft robot manipulations". In: *The International Journal of Advanced Manufacturing Technology* 80 (Apr. 2015). DOI: 10.1007/s00170-015-7085-3.

[23] Aslan Miriyev, Kenneth Stack, and Hod Lipson. "Soft material for soft actuators". In: *Nature Communications* 8 (Dec. 2017). DOI: 10.1038/s41467-017-00685-3.

[24] Carmel Majidi. "Soft Robotics: A Perspective—Current Trends and Prospects for the Future". In: *Soft Robotics* 1 (Mar. 2014), pp. 5–11. DOI: 10.1089/soro.2013.0001.

[25] Mariangela Manti, Vito Cacucciolo, and Matteo Cianchetti. "Stiffening in Soft Robotics: A Review of the State of the Art". In: *IEEE Robotics Automation Magazine* 23 (Sept. 2016), pp. 93–106. DOI: 10.1109/MRA.2016.2582718.

[26] Giorgio Grioli et al. "Variable stiffness actuators: The user's point of view". In: *The International Journal of Robotics Research* 34.6 (2015), pp. 727–743. DOI: 10.1177/0278364914566515. eprint: https://doi.org/10.1177/0278364914566515. URL: https://doi.org/10.1177/0278364914566515.

[27] B. Vanderborght et al. "Variable impedance actuators: A review". In: *Robotics and Autonomous Systems* 61.12 (2013), pp. 1601–1614. ISSN: 0921-8890. DOI: https://doi.org/10.1016/j.robot.2013.06.009. URL: http://www.sciencedirect.com/science/article/pii/S0921889013001188.

[28] Sebastian Wolf et al. "Soft Robotics with Variable Stiffness Actuators: Tough Robots for Soft Human Robot Interaction". In: *Soft Robotics*. Ed. by Alexander Verl et al. Berlin, Heidelberg: Springer Berlin Heidelberg, 2015, pp. 231–254. ISBN: 978-3-662-44506-8.

[29] A. Stilli, H. A. Wurdemann, and K. Althoefer. "Shrinkable, stiffness-controllable soft manipulator based on a bio-inspired antagonistic actuation principle". In: *2014 IEEE/RSJ International Conference on Intelligent Robots and Systems*. Sept. 2014, pp. 2476–2481. DOI: 10.1109/IROS.2014.6942899.

[30] F. Maghooa et al. "Tendon and pressure actuation for a bio-inspired manipulator based on an antagonistic principle". In: *2015 IEEE International Conference on Robotics and Automation (ICRA)*. May 2015, pp. 2556–2561. DOI: 10.1109/ICRA.2015.7139542.

[31] A. Shiva et al. "Tendon-Based Stiffening for a Pneumatically Actuated Soft Manipulator". In: *IEEE Robotics and Automation Letters* 1.2 (July 2016), pp. 632–637. ISSN: 2377-3774. DOI: 10.1109/LRA.2016.2523120.

[32] Cecilia Laschi et al. “Design of a biomimetic robotic octopus arm”. In: *Bioinspiration biomimetics* 4 (Apr. 2009), p. 015006. DOI: 10.1088/1748-3182/4/1/015006.

[33] Cecilia Laschi et al. “Soft Robot Arm Inspired by the Octopus”. In: *Advanced Robotics* 26.7 (2012), pp. 709–727. DOI: 10.1163/156855312X626343. eprint: https://doi.org/10.1163/156855312X626343. URL: https://doi.org/10.1163/156855312X626343.

[34] Matteo Cianchetti et al. “Bioinspired Soft Actuation System Using Shape Memory Alloys”. In: *Actuators* 3 (Sept. 2014), pp. 226–244. DOI: 10.3390/act3030226.

[35] Federico Carpi et al. “Enabling variable-stiffness hand rehabilitation orthoses with dielectric elastomer transducers”. In: *Medical Engineering Physics* 36.2 (2014), pp. 205–211. ISSN: 1350-4533. DOI: https://doi.org/10.1016/j.medengphy.2013.10.015. URL: http://www.sciencedirect.com/science/article/pii/S1350453313002361.

[36] Markus Henke, Jörg Sorber, and Gerald Gerlach. “Multi-layer beam with variable stiffness based on electroactive polymers”. In: vol. 8340. Society of Photo-Optical Instrumentation Engineers (SPIE) Conference Series. 2012, 83401P. DOI: 10.1117/12.915138.

[37] Jun Ya Nagase et al. “Design of a variable-stiffness robotic hand using pneumatic soft rubber actuators”. English. In: *Smart Materials and Structures* 20.10 (Oct. 2011). ISSN: 0964-1726. DOI: 10.1088/0964-1726/20/10/105015.

[38] S. Wakimoto, I. Kumagai, and K. Suzumori. “Development of large intestine endoscope changing its stiffness”. In: *2009 IEEE International Conference on Robotics and Biomimetics (ROBIO)*. Dec. 2009, pp. 2320–2325. DOI: 10.1109/ROBIO.2009.5420727.

[39] J. R. Amend et al. “A Positive Pressure Universal Gripper Based on the Jamming of Granular Material”. In: *IEEE Transactions on Robotics* 28.2 (Apr. 2012), pp. 341–350. ISSN: 1941-0468. DOI: 10.1109/TRO.2011.2171093.

[40] N. G. Cheng et al. “Design and Analysis of a Robust, Low-cost, Highly Articulated manipulator enabled by jamming of granular media”. In: *2012 IEEE International Conference on Robotics and Automation*. May 2012, pp. 4328–4333. DOI: 10.1109/ICRA.2012.6225373.

[41] Yashraj Narang, Joost Vlassak, and Robert Howe. “Mechanically Versatile Soft Machines through Laminar Jamming”. In: *Advanced Functional Materials* 28 (Feb. 2018), p. 1707136. DOI: 10.1002/adfm.201707136.

[42] Y. S. Narang et al. “Transforming the Dynamic Response of Robotic Structures and Systems Through Laminar Jamming”. In: *IEEE Robotics and Automation Letters* 3.2 (Apr. 2018), pp. 688–695. ISSN: 2377-3774. DOI: 10.1109/LRA.2017.2779802.

[43] Carmel Majidi and Robert J. Wood. "Tunable elastic stiffness with microconfined magnetorheological domains at low magnetic field". In: *Applied Physics Letters* 97.16 (2010), p. 164104. DOI: 10.1063/1.3503969. eprint: https://doi.org/10.1063/1.3503969. URL: https://doi.org/10.1063/1.3503969.

[44] J.David Carlson and Mark R Jolly. "MR fluid, foam and elastomer devices". In: *Mechatronics* 10.4 (2000), pp. 555–569. ISSN: 0957-4158. DOI: https://doi.org/10.1016/S0957-4158(99)00064-1. URL: http://www.sciencedirect.com/science/article/pii/S0957415899000641.

[45] Wanliang Shan et al. "Rigidity-tuning conductive elastomer". In: *Smart Materials and Structures* 24.6 (May 2015), p. 065001. DOI: 10.1088/0964-1726/24/6/065001. URL: https://doi.org/10.1088%2F0964-1726%2F24%2F6%2F065001.

[46] C Santulli et al. "Development of smart variable stiffness actuators using polymer hydrogels". In: *Smart Materials and Structures* 14.2 (Mar. 2005), pp. 434–440. DOI: 10.1088/0964-1726/14/2/018. URL: https://doi.org/10.1088%2F0964-1726%2F14%2F2%2F018.

[47] Michael Andrew McEvoy, Nicholas Farrow, and Nikolaus Correll. "Robotic materials with controllable stiffness". In: *The 19th International Conference on Composite Materials (ICCM)*. July 2013. URL: https://pdfs.semanticscholar.org/2a6b/a45ff15044bea4e38bd7298564ba30b6bb65.pdf.

[48] Nadia G. Cheng et al. "Thermally Tunable, Self-Healing Composites for Soft Robotic Applications". In: *Macromolecular Materials and Engineering* 299.11 (2014), pp. 1279–1284. DOI: 10.1002/mame.201400017. eprint: https://www.onlinelibrary.wiley.com/doi/pdf/10.1002/mame.201400017. URL: https://www.onlinelibrary.wiley.com/doi/abs/10.1002/mame.201400017.

[49] M Andy McEvoy and Nikolaus Correll. "Thermoplastic variable stiffness composites with embedded, networked sensing, actuation, and control". In: *Journal of Composite Materials* 49.15 (2015), pp. 1799–1808. DOI: 10.1177/0021998314525982. eprint: https://doi.org/10.1177/0021998314525982. URL: https://doi.org/10.1177/0021998314525982.

[50] Jeffrey R. Capadona et al. "Stimuli-Responsive Polymer Nanocomposites Inspired by the Sea Cucumber Dermis". In: *Science* 319.5868 (2008), pp. 1370–1374. ISSN: 0036-8075. DOI: 10.1126/science.1153307. eprint: https://science.sciencemag.org/content/319/5868/1370.full.pdf. URL: https://science.sciencemag.org/content/319/5868/1370.

[51] Bryan E. Schubert and Dario Floreano. "Variable stiffness material based on rigid low-melting-point-alloy microstructures embedded in soft poly(dimethylsiloxane) (PDMS)". In: *RSC Adv.* 3 (46 2013), pp. 24671–24679. DOI: 10.1039/C3RA44412K. URL: http://dx.doi.org/10.1039/C3RA44412K.

[52] Farhan Gandhi and Sang-Guk Kang. "Beams with controllable flexural stiffness". In: *Smart Materials and Structures* 16.4 (June 2007), pp. 1179–1184. DOI: 10.1088/0964-1726/16/4/028. URL: https://doi.org/10.1088%2F0964-1726%2F16%2F4%2F028.

[53] Emily A. Allen, Lee D. Taylor, and John P. Swensen. "Smart material composites for discrete stiffness materials". In: *Smart Material Structures* 28.7, 074007 (July 2019), p. 074007. DOI: 10.1088/1361-665X/ab1ec9.

[54] Knut Schmidt-Nielsen. *Animal physiology: adaptation and environment.* Cambridge University Press, 1997.

[55] William Kier and Kathleen Smith. "Tongues, tentacles and trunks: the biomechanics of movement in muscular-hydrostats". In: *Zoological Journal of the Linnean Society* 83 (Apr. 1985), pp. 307–324. DOI: 10.1111/j.1096-3642.1985.tb01178.x.

[56] Andrew D. Horchler et al. "Worm-Like Robotic Locomotion with a Compliant Modular Mesh". In: *Biomimetic and Biohybrid Systems.* Ed. by Stuart P. Wilson et al. Cham: Springer International Publishing, 2015, pp. 26–37.

[57] Auke J. Ijspeert. "Biorobotics: Using robots to emulate and investigate agile locomotion". In: *Science* 346.6206 (2014), pp. 196–203. ISSN: 0036-8075. DOI: 10.1126/science.1254486. eprint: http://science.sciencemag.org/content/346/6206/196.full.pdf. URL: http://science.sciencemag.org/content/346/6206/196.

[58] Stefano Palagi et al. "Structured light enables biomimetic swimming and versatile locomotion of photoresponsive soft microrobots". In: *Nature Materials* advance online publication (Feb. 2016). DOI: 10.1038/nmat4569.

[59] Giovanni Tonietti, Riccardo Schiavi, and Antonio Bicchi. "Design and control of a variable stiffness actuator for safe and fast physical human/robot interaction". In: *Robotics and Automation, 2005. ICRA 2005. Proceedings of the 2005 IEEE International Conference on.* IEEE. 2005, pp. 526–531.

[60] Riccardo Schiavi et al. "VSA-II: a novel prototype of variable stiffness actuator for safe and performing robots interacting with humans". In: *Robotics and Automation, 2008. ICRA 2008. IEEE International Conference on.* IEEE. 2008, pp. 2171–2176.

[61] Nikos G Tsagarakis, Irene Sardellitti, and Darwin G Caldwell. "A new variable stiffness actuator (CompAct-VSA): Design and modelling". In: *Intelligent Robots and Systems (IROS), 2011 IEEE/RSJ International Conference on.* IEEE. 2011, pp. 378–383.

[62] Nevio Luigi Tagliamonte et al. "Double actuation architectures for rendering variable impedance in compliant robots: A review". In: *Mechatronics* 22.8 (2012), pp. 1187–1203.

[63] Chandana Paul et al. "Gait production in a tensegrity based robot". In: *ICAR'05. Proceedings., 12th International Conference on Advanced Robotics, 2005.* IEEE. 2005, pp. 216–222.

[64] Mizuho Shibata, Fumio Saijyo, and Shinichi Hirai. "Crawling by body deformation of tensegrity structure robots". In: *Robotics and Automation, 2009. ICRA'09. IEEE International Conference on.* IEEE. 2009, pp. 4375–4380.

[65] Atil Iscen et al. "Controlling tensegrity robots through evolution". In: *Proceedings of the 15th annual conference on Genetic and evolutionary computation.* ACM. 2013, pp. 1293–1300.

[66] Chandana Paul, Francisco J Valero-Cuevas, and Hod Lipson. "Design and control of tensegrity robots for locomotion". In: *IEEE Transactions on Robotics* 22.5 (2006), pp. 944–957.

[67] Frank Daerden and Dirk Lefeber. "Pneumatic artificial muscles: actuators for robotics and automation". In: *European journal of mechanical and environmental engineering* 47.1 (2002), pp. 11–21.

[68] Pieter Beyl et al. "Pleated Pneumatic Artificial Muscle-Based Actuator System as a Torque Source for Compliant Lower Limb Exoskeletons". In: *Mechatronics, IEEE/ASME Transactions on* 19.3 (2014), pp. 1046–1056.

[69] J. Avery et al. "Shape Sensing of Variable Stiffness Soft Robots using Electrical Impedance Tomography". In: *arXiv e-prints* (Apr. 2019). arXiv: 1904.02429 `[cs.RO]`.

[70] A. A. M. Faudzi et al. "Development of bending soft actuator with different braided angles". In: *2012 IEEE/ASME International Conference on Advanced Intelligent Mechatronics (AIM).* July 2012, pp. 1093–1098.

[71] A. A. Mohd Faudzi et al. "Index Finger of a Human-Like Robotic Hand Using Thin Soft Muscles". In: *IEEE Robotics and Automation Letters* 3.1 (Jan. 2018), pp. 92–99. ISSN: 2377-3766. DOI: 10.1109/LRA.2017.2732059.

[72] A. Garriga-Casanovas et al. "Multifilament pneumatic artificial muscles to mimic the human neck". In: *2017 IEEE International Conference on Robotics and Biomimetics (ROBIO).* Dec. 2017, pp. 809–816. DOI: 10.1109/ROBIO.2017.8324517.

[73] Loai A.T. Al Abeach, Samia Nefti-Meziani, and Steve Davis. "Design of a Variable Stiffness Soft Dexterous Gripper". In: *Soft Robotics* 4.3 (2017). PMID: 29062630, pp. 274–284. DOI: 10.1089/soro.2016.0044. eprint: https://doi.org/10.1089/soro.2016.0044. URL: https://doi.org/10.1089/soro.2016.0044.

[74] Changquing Li and Christopher D Rahn. "Design of continuous backbone, cable-driven robots". In: *Journal of Mechanical Design* 124.2 (2002), pp. 265–271.

[75] Michael W Hannan and Ian D Walker. “Kinematics and the implementation of an elephant’s trunk manipulator and other continuum style robots”. In: *Journal of Robotic Systems* 20.2 (2003), pp. 45–63.

[76] Marcello Calisti et al. “An octopus-bioinspired solution to movement and manipulation for soft robots”. In: *Bioinspiration & biomimetics* 6.3 (2011), p. 036002.

[77] Evan Vander Hoff, Donghwa Jeong, and Kiju Lee. “OrigamiBot-I: A thread-actuated origami robot for manipulation and locomotion”. In: *2014 IEEE/RSJ International Conference on Intelligent Robots and Systems*. IEEE. 2014, pp. 1421–1426.

[78] Wanliang Shan, Tong Lu, and Carmel Majidi. “Soft-matter composites with electrically tunable elastic rigidity”. In: *Smart Materials and Structures* 22.8 (2013), p. 085005.

[79] Wei Wang, Hugo Rodrigue, and Sung-Hoon Ahn. “Smart soft composite actuator with shape retention capability using embedded fusible alloy structures”. In: *Composites Part B: Engineering* 78 (2015), pp. 507–514.

[80] J. Shintake et al. “Variable stiffness actuator for soft robotics using dielectric elastomer and low-melting-point alloy”. In: *2015 IEEE/RSJ International Conference on Intelligent Robots and Systems (IROS)*. Sept. 2015, pp. 1097–1102. DOI: 10.1109/IROS.2015.7353507.

[81] Thomas P Chenal et al. “Variable stiffness fabrics with embedded shape memory materials for wearable applications”. In: *Intelligent Robots and Systems (IROS 2014), 2014 IEEE/RSJ International Conference on*. IEEE. 2014, pp. 2827–2831.

[82] M. C. Yuen, R. A. Bilodeau, and R. K. Kramer. “Active Variable Stiffness Fibers for Multifunctional Robotic Fabrics”. In: *IEEE Robotics and Automation Letters* 1.2 (July 2016), pp. 708–715. ISSN: 2377-3766. DOI: 10.1109/LRA.2016.2519609.

[83] Wei Wang and Sung-Hoon Ahn. “Shape Memory Alloy-Based Soft Gripper with Variable Stiffness for Compliant and Effective Grasping”. In: *Soft Robotics* 4 (Oct. 2017). DOI: 10.1089/soro.2016.0081.

[84] *ISO 7438:2005(E): Metallic materials – Bend test*. Standard. June 2005.

[85] *ASTM D790-03 – Standard Test Methods for Flexural Properties of Unreinforced and Reinforced Plastics and Electrical Insulating Materials*. Standard. ATSM International, 2003. DOI: 10.1520/D0790-03.

[86] Hong Kai Yap, Hui Yong Ng, and Raye Chen-Hua Yeow. “High-Force Soft Printable Pneumatics for Soft Robotic Applications”. In: *Soft Robotics* 3 (Sept. 2016), pp. 144–158. DOI: 10.1089/soro.2016.0030.

[87] Guang-Zhong Yang et al. "The grand challenges of Science Robotics". In: *Science Robotics* 3.14 (2018). DOI: 10.1126/scirobotics.aar7650. URL: http://robotics.sciencemag.org/content/3/14/eaar7650.

[88] Ali Zolfagharian et al. "Pattern-driven 4D printing". In: *Sensors and Actuators A: Physical* 274 (2018), pp. 231–243. ISSN: 0924-4247. DOI: https://doi.org/10.1016/j.sna.2018.03.034. URL: http://www.sciencedirect.com/science/article/pii/S0924424718300621.

[89] Jheng-Wun Su et al. "4D printing of a self-morphing polymer driven by a swellable guest medium". In: *Soft Matter* 14 (5 2018), pp. 765–772. DOI: 10.1039/C7SM01796K. URL: http://dx.doi.org/10.1039/C7SM01796K.

[90] Aslan Miriyev, Gabriela Caires, and Hod Lipson. "Functional properties of silicone/ethanol soft-actuator composites". In: *Materials & Design* 145 (2018), pp. 232–242. ISSN: 0264-1275. DOI: https://doi.org/10.1016/j.matdes.2018.02.057. URL: http://www.sciencedirect.com/science/article/pii/S0264127518301485.

[91] D Rus and M Tolley. "Design, fabrication and control of soft robots". In: *Nature* 521.7553 (2015), pp. 467–475.

[92] P. Polygerinos et al. "Modeling of Soft Fiber-Reinforced Bending Actuators". In: *IEEE Transactions on Robotics* 31.3 (June 2015), pp. 778–789. DOI: 10.1109/TRO.2015.2428504.

[93] Ning Tan, Xiaoyi Gu, and Hongliang Ren. "Design, characterization and applications of a novel soft actuator driven by flexible shafts". In: *Mechanism and Machine Theory* 122 (2018), pp. 197–218. ISSN: 0094-114X. DOI: https://doi.org/10.1016/j.mechmachtheory.2017.12.021. URL: http://www.sciencedirect.com/science/article/pii/S0094114X1731087X.

[94] Emily A Allen, Lee D Taylor, and John P Swensen. "Smart Material Composites for Discrete Stiffness Materials". In: *Proc. ASME 2018 Conference on Smart Materials, Adaptive Structures and Intelligent Systems (SMASIS2018)*. San Antonio, TX, Sept. 2018, V002T06A015.

[95] Michael McEvoy and Nikolaus Correll. "Shape Change Through Programmable Stiffness". In: vol. 109. ISER, Jan. 2016, pp. 893–907. DOI: 10.1007/978-3-319-23778-7_59.

[96] J Swensen et al. "Printing Three-Dimensional Electrical Traces in Additive Manufactured Parts for Injection of Low Melting Temperature Metals". In: *Journal of Mechanisms and Robotics* 7.2 (2015), pp. 021004–021004.

[97] Richard M. Murray, Zexiang Li, and S. Shankara Sastry. *A mathematical introduction to robotic manipulation.* CRC Press, 1994.

[98] Larry L Howell. *Compliant mechanisms.* John Wiley & Sons, 2001.

[99] Mark Runciman, Ara Darzi, and George P. Mylonas. "Soft Robotics in Minimally Invasive Surgery". In: *Soft robotics* 6.4 (Aug. 2019), pp. 423–443. ISSN: 2169-5180. DOI: 10.1089/soro.2018.0136. URL: https://www.ncbi.nlm.nih.gov/pubmed/30920355.

[100] Cecilia Laschi, Barbara Mazzolai, and Matteo Cianchetti. "Soft robotics: Technologies and systems pushing the boundaries of robot abilities". In: *Science Robotics* 1.1 (2016). DOI: 10.1126/scirobotics.aah3690.

[101] Laura Margheri et al. "Bio-inspired Design of an Artificial Muscular-Hydrostat Unit for Soft Robotic Systems". In: vol. 7375. July 2012, pp. 375–376. DOI: 10.1007/978-3-642-31525-1_49.

[102] Yunquan Li et al. "Precharged Pneumatic Soft Actuators and Their Applications to Untethered Soft Robots". In: *Soft Robotics* 5.5 (2018). PMID: 29924683, pp. 567–575. DOI: 10.1089/soro.2017.0090. eprint: https://doi.org/10.1089/soro.2017.0090. URL: https://doi.org/10.1089/soro.2017.0090.

[103] Andrew D. Marchese, Robert K. Katzschmann, and Daniela Rus. "A Recipe for Soft Fluidic Elastomer Robots". In: *Soft Robotics* 2.1 (2015). PMID: 27625913, pp. 7–25. DOI: 10.1089/soro.2014.0022. eprint: https://doi.org/10.1089/soro.2014.0022. URL: https://doi.org/10.1089/soro.2014.0022.

[104] J. D. W. Madden et al. "Artificial muscle technology: physical principles and naval prospects". In: *IEEE Journal of Oceanic Engineering* 29.3 (July 2004), pp. 706–728. DOI: 10.1109/JOE.2004.833135.

[105] T. Doi et al. "Proposal of flexible robotic arm with thin McKibben actuators mimicking octopus arm structure". In: *2016 IEEE/RSJ International Conference on Intelligent Robots and Systems (IROS).* Oct. 2016, pp. 5503–5508. DOI: 10.1109/IROS.2016.7759809.

[106] Shota Furukawa et al. "A Soft Master-Slave Robot Mimicking Octopus Arm Structure Using Thin Artificial Muscles and Wire Encoders". In: *Actuators* 8 (May 2019), p. 40. DOI: 10.3390/act8020040.

[107] Daniël Villegas Casi et al. "Third Generation Pleated Pneumatic Artificial Muscles for Robotic Applications: Development and Comparison with McKibben Muscle". English. In: *Advanced Robotics* 26.11-12 (July 2012), pp. 1205–1227. ISSN: 0169-1864.

[108] Benjamin Gorissen et al. "Elastic Inflatable Actuators for Soft Robotic Applications". In: *Advanced Materials* 29 (Sept. 2017), p. 1604977. DOI: 10.1002/adma.201604977.

[109] George M. Whitesides. "Soft Robotics". In: *Angewandte Chemie International Edition* 57.16 (2018), pp. 4258–4273. DOI: 10.1002/anie.201800907. eprint: https://

onlinelibrary.wiley.com/doi/pdf/10.1002/anie.201800907. URL: https://onlinelibrary.wiley.com/doi/abs/10.1002/anie.201800907.

[110] R. Praneeth et al. “Design, Analysis, Manufacturing and Testing of Artificial Hand with Fingers made of Rubber Actuators”. In: *Materials Today: Proceedings* 5.11, Part 3 (2018), pp. 25236–25244. ISSN: 2214-7853. DOI: https://doi.org/10.1016/j.matpr.2018.10.326. URL: http://www.sciencedirect.com/science/article/pii/S2214785318326300.

[111] Filip Ilievski et al. “Soft Robotics for Chemists”. In: *Angewandte Chemie* 123.8 (2011), pp. 1930–1935.

[112] Ramses V. Martinez et al. “Robotic Tentacles with Three-Dimensional Mobility Based on Flexible Elastomers”. In: *Advanced Materials* 25.2 (2013), pp. 205–212. DOI: 10.1002/adma.201203002. eprint: https://onlinelibrary.wiley.com/doi/pdf/10.1002/adma.201203002. URL: https://onlinelibrary.wiley.com/doi/abs/10.1002/adma.201203002.

[113] Yuan-Fang Zhang et al. “Miniature Pneumatic Actuators for Soft Robots by High-Resolution Multimaterial 3D Printing”. In: *Advanced Materials Technologies* 0.0 (), p. 1900427. DOI: 10.1002/admt.201900427. eprint: https://onlinelibrary.wiley.com/doi/pdf/10.1002/admt.201900427. URL: https://onlinelibrary.wiley.com/doi/abs/10.1002/admt.201900427.

[114] Fionnuala Connolly et al. “Mechanical programming of soft actuators by varying fiber angle”. English (US). In: *Soft Robotics* 2.1 (Mar. 2015), pp. 26–32. ISSN: 2169-5172. DOI: 10.1089/soro.2015.0001.

[115] J. Bishop-Moser et al. “Design of soft robotic actuators using fluid-filled fiber-reinforced elastomeric enclosures in parallel combinations”. In: *2012 IEEE/RSJ International Conference on Intelligent Robots and Systems*. Oct. 2012, pp. 4264–4269. DOI: 10.1109/IROS.2012.6385966.

[116] Raphael Deimel and Oliver Brock. “A compliant hand based on a novel pneumatic actuator”. In: *2013 IEEE International Conference on Robotics and Automation* (2013), pp. 2047–2053.

[117] Hironari Taniguchi. “Flexible Artificial Muscle Actuator Using Coiled Shape Memory Alloy Wires”. In: *APCBEE Procedia* 7 (2013). The 3rd International Conference on Biomedical Engineering and Technology - ICBET 2013, pp. 54–59. ISSN: 2212-6708. DOI: https://doi.org/10.1016/j.apcbee.2013.08.012. URL: http://www.sciencedirect.com/science/article/pii/S2212670813001140.

[118] Joan Ortega Alcaide, Levi Pearson, and Mark Rentschler. “Design, modeling and control of a SMA-actuated biomimetic robot with novel functional skin”. In: *2017 IEEE International Conference on Robotics and Automation (ICRA)* (2017), pp. 4338–4345.

APPENDIX

Appendix A

COMPRESSION/TENSION DATA FOR SILICONE MATERIAL AND NITINOL SPRINGS

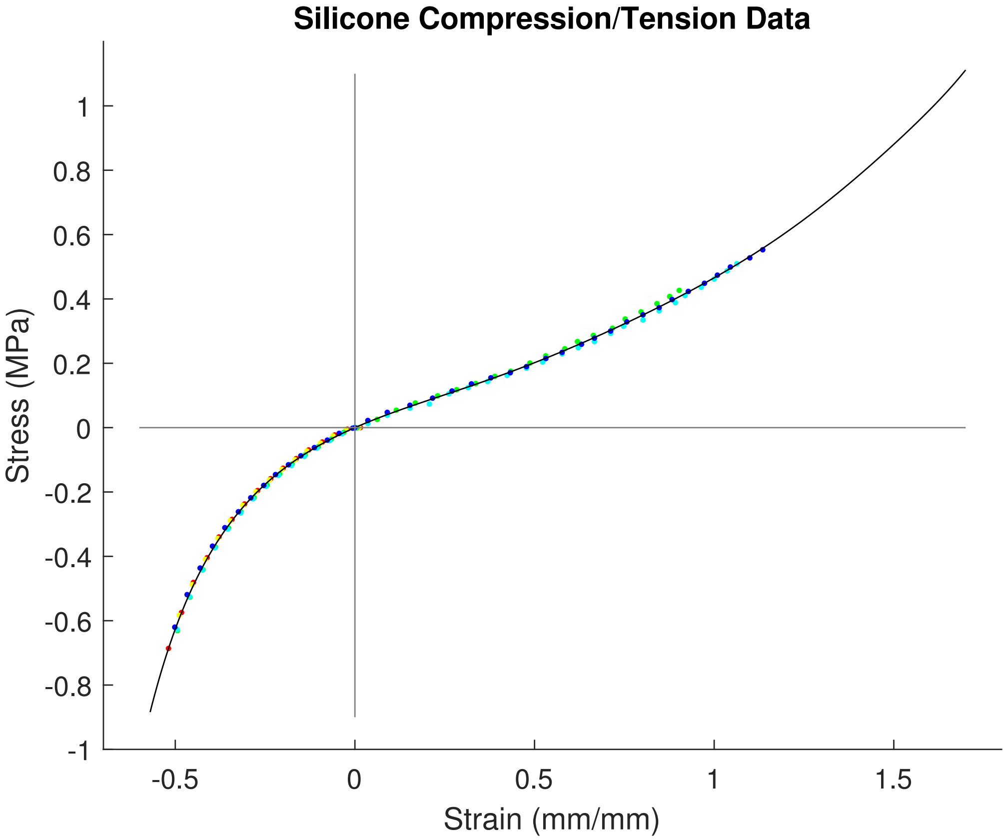

Figure A.1 Silicone compression and tension test data with 9th order polynomial curve fit for computing secant modulus of elasticity.

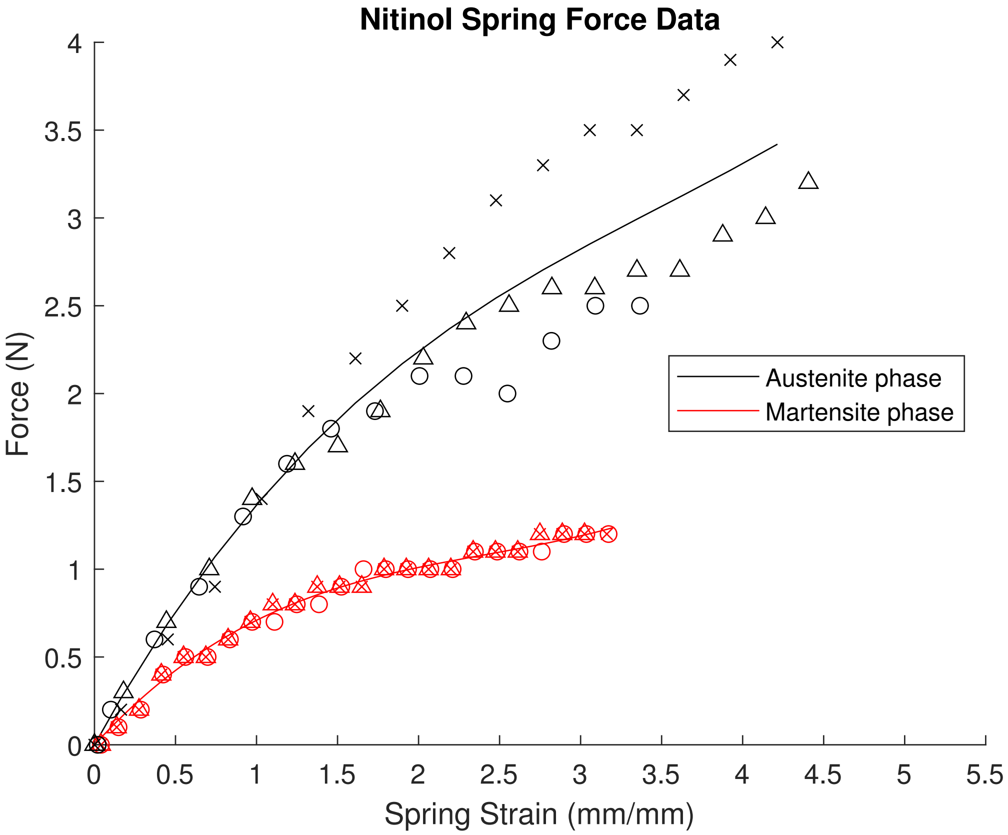

Figure A.2 Nitinol spring tension test data with 3rd order polynomial curve fit for computing secant modulus of elasticity.